5-2016

Exploiting Stiffness Nonlinearities to Improve the Performance of Galloping Flow Energy Harvesters

Ali H. Alhadidi
Clemson University

EXPLOITING STIFFNESS NONLINEARITIES TO IMPROVE THE PERFORMANCE OF GALLOPING FLOW ENERGY HARVESTERS

A Dissertation

Presented to

the Graduate School of

Clemson University

---

in Partial Fulfillment

of the Requirements for the Degree

Doctor of Philosophy

Mechanical Engineering

By

Ali H. Alhadidi

May 2016

Dr. Mohammed F. Daqaq, Committee Chair

Dr. Gang Li

Dr. Nicole Coutris

Dr. Phanindra Tallapragada

Abstract

Fluid-structure coupling mechanisms such as galloping and wake galloping have recently emerged as effective methods to develop scalable flow energy harvesters (FEHs) that can be used to power remote sensors and sensor networks. The operation concept of these devices is based on coupling the pressure forces culminating from the motion of the fluid past a mechanical oscillator to its natural modes of vibration. As a result, the mechanical oscillator undergoes large-amplitude motions that can be transformed into electricity by utilizing an electromechanical transduction mechanism, which is generally piezoelectric or electromagnetic in nature. Due to their scalability and design simplicity, FEHs are believed to be more effective for micro-power generation than their traditional rotary-type counterparts whose efficiency is known to drop significantly as their size decreases. Furthermore, FEHs can be used to harvest energy from unsteady flow patterns which permits targeting a niche market that traditional rotary-type generators do not address.

In the open literature, galloping FEHs have always been designed to possess a linear restoring force. This dissertation considers the design and performance analysis of galloping FEHs with a nonlinear restoring force. Specifically, the objective of this dissertation is three fold. First, it assesses the influence of stiffness nonlinearities on the performance of galloping FEHs under steady and laminar flow conditions. Second, it studies the influence of the nonlinearity on the response of a wake galloping FEH to single- and multi-frequency Von Karman vortex streets. Third, for known flow characteristics, the dissertation provides directions for how to choose the restoring force of the harvester to maximize the output power. To achieve the objectives of this dissertation, a nonlinear FEH which consists of a thin piezoelectric cantilever beam augmented with a square-sectioned bluff body at the free end is considered. Two magnets located near the tip of the bluff body are used to introduce the nonlinearity which strength and nature can be altered by changing the distance

between the magnets.

For a steady laminar flow, three types of nonlinear restoring forces are compared: bi-stable, mono-stable hardening, and mono-stable softening. To study the influence of the restoring force on the performance, a physics-based nonlinear lumped-parameter aero-electromechanical model adopting the quasi-steady assumption for aerodynamic loading is developed. A closed-form solution of the nonlinear response is obtained by employing a multiple-scales perturbation analysis using the Jacobi elliptic functions. The attained solution is validated experimentally using wind tunnel tests performed at different wind speeds for the three types of restoring forces considered. The validated solution is then used to study the influence of the nonlinearity on the harvesters response. In general, it is shown that, under optimal operating conditions, a harvester designed with a bi-stable restoring force outperforms the other designs.

For single- and multi-frequency vortex streets, only linear and bi-stable restoring forces were considered and compared. A nonlinear lumped-parameter model adopting the common uncoupled single-frequency force model for aerodynamics loading is developed and solved using the method of multiple scales. The model is validated against experimental data obtained in a wind tunnel. It is demonstrated that when subjected to a single-frequency periodic wake, the broadband characteristics of wake-galloping FEHs can be dramatically improved by incorporating a bi-stable restoring force. This has the influence of reducing the harvester's sensitivity to variations in the wind speed around the nominal design value. It is also demonstrated that the shape of the potential function has a considerable influence on the performance of the bi-stable wake galloping FEH. Specifically, it is shown that, for shallower potential wells and smaller separation distances between the wells, the harvester starts performing large inter-well motions at lower wind speeds, but the resulting inter-well motions are generally smaller. On the other hand, for deeper potential wells and larger separation distances between the wells, the harvester starts performing

large inter-well motions at higher wind speeds, but the magnitude of the resulting inter-well motions are generally larger.

The dissertation also compared the performance of linear and bi-stable wake-galloping FEHs under a multi-frequency vortex street. Results demonstrated that the bi-stable system outperforms the linear harvester as long as the vortices have sufficient time to interact and build a multi-frequency vortical structure. Maximum voltage levels were generated at locations where the interacting vortices result in powerful modes close to the harvesters natural frequency.

Dedication

To my lovely parents, for their endless love, encouragement, and support.

Acknowledgments

First, I would like to thank God for everything He bestowed upon me.

My deepest gratitude goes to my advisor, Dr. Mohammed F. Daqaq, who walked me gracefully through this whole experience; for his endless help and support. I am honored to have him as my friend and mentor, who supplied many answers while helping me through this work.

Special thanks also go to my committee members, Dr. Gang Li, Dr. Nicole Coutris, and Dr. Phanindra Tallapragada for their constructive and encouraging feedback; and to all professors I have taken courses with: Dr. Vincent Ervin, Dr. Mohammed Daqaq, Dr. Harry Law, Dr. Adrlan Vahedi, Dr. Timothy Burg, and Dr. Richard Miller.

Words of appreciation are due to my great circle of friends and colleagues; particularly those who offered me help during my stay in Clemson; advice, and good encouragement while I was working on my research: Samer Alomar, Steven Canaday, Dr. Amin Bibo, Dr. Malek Aljamlyeh, Saad Alazmi, Dr. Megashyam Pynyam, Qifan He, Nicholas Caldwell, Abdalrouf Abusoua, Yawen Xu, Jamie Noel, and Clodoaldo Silva.

Finally, much love and appreciation to my family, my faithful parents, Haitham Alhadidi and Maysoon Alsaket, who have encouraged me to pursue my Ph.D; my brothers Omar and Abdullah, my sisters Dema, Doaa and Sabaa, my brothers-in-law Mohammed Alzoubi and Khaled Abu Alghanam, and my sister-in-law Dana Alkhawatreh, for their continuous encouragement and support.

Contents

List of Figures

List of Tables

Chapter 1

Introduction

1.1 Motivations

Exploiting ambient energy and converting it into a useful form is an old concept which humans have depended on for many centuries to meet their basic energy needs. Water wheels and windmills are a few examples of how people used to convert flow energy and wind into useful power [1, 2]. By the end of the nineteenth century, and as a result of the discovery of Faraday's law of induction, these technologies evolved and were used to convert ambient energy into electrical power. Currently, about 19% of total electricity production in the world comes from hydropower and around 3% results from wind turbines [3].

Today, we are exploring these same concepts to maintain low-power electronic devices which, in light of recent advances in electronic circuit design and microfabrications technologies, have evolved to function with minimum power levels. Examples of such devices include, but are not limited to, structural health-monitoring sensors [4, 5], wireless sensor networks for ecological, geological, and climate studies [6, 7, 8], and medical implants [9, 10, 11, 12]. The majority of such devices currenlty depend

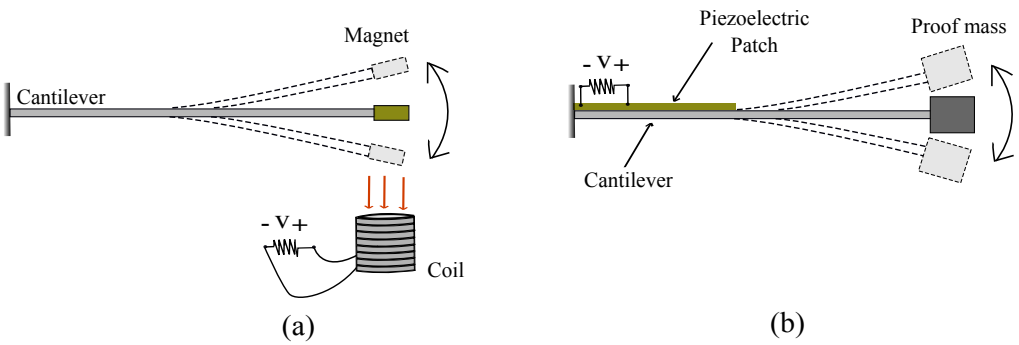

Figure 1.1: Schematics of: (a) typical electromagnetic energy harvester, and (b) typical piezoelectric energy harvester.

on batteries which have limited life span, and require regular replacement and/or recharging which can be a cumbersome and costly process especially in remote and hard-to-access locations [9].

To overcome this problem, various scalable methods have been recently proposed to scavenge wasted ambient energy and convert it into usable power. Among these methods, vibratory and flow energy harvesting have flourished as major thrust areas. In vibratory energy harvesting, a mechanical oscillator, similar to the cantilever beam shown in Fig. 1.1, is set into motion via external base excitations [13, 14, 15, 16, 17, 18, 19, 20, 21, 22]. The motion of the beam is then used to produce electricity via electromagnetic induction as shown in Fig. 1.1(a), or by straining a piezoelectric element laminated at its base as shown in Fig. 1.1(b).

In flow energy harvesting, a mechanical oscillator, again similar to the beam shown in Fig. 1.1, is set into motion as a result of the coupling between the pressure forces culminating from the motion of the fluid past the oscillator and its natural modes of vibration. As a result of this coupling, the mechanical oscillator undergoes large-amplitude deflections that can be transformed into electricity by utilizing an electromechanical transduction mechanism, which is generally piezoelectric or electromagnetic in nature.

As a result of the simplicity of these new designs, this approach is believed to be more effective for small-scale applications than the traditional hydroelectric and wind turbines which utilize rotary-type generators to transform mechanical motions into electricity. Furthermore, the efficiency of rotary-type generators drops significantly as their size decreases [23, 24]. This stems from their complex design, electromagnetic interferences, and mechanical losses such as friction and bearing losses which become dominant as size decreases. As a result, their implementation for low-power applications is limited [25, 26, 27]. Figure. 1.2 depicts a classification of various energy harvesting methods based on the vibration source, and the electro-mechanical transduction method.

1.2 Flow Energy Harvesting

In flow energy harvesting, motion of the mechanical oscillator results from different instabilities that can be classified based on the nature of the flow pattern around

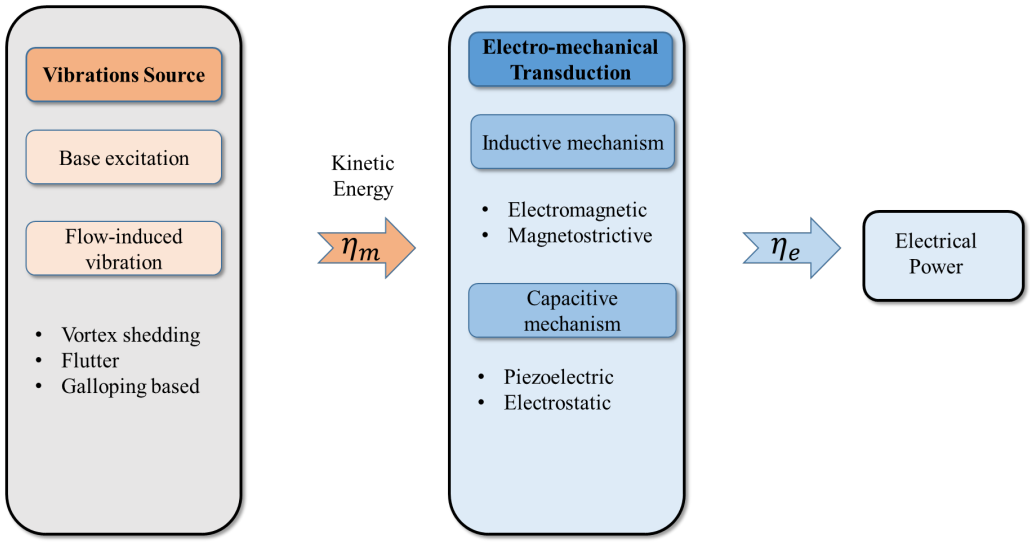

Figure 1.2: Classification of various energy harvesting methods based on vibration source and electromechanical transduction method.

the structure. As shown in Fig. 1.3, three different mechanisms can be used to set the oscillator into motion. These are wake-galloping, galloping, and flutter.

Wake-galloping is known to occur when an obstacle is located in the upstream of the harvester. As shown if Fig. 1.3 (a), when air flows past the obstacle, it can create a Von Kármán vortex street which in turn, generates oscillating pressure forces in the leeward side of the bluff body. This causes the harvester to vibrate in a periodic pattern when the vortex shedding is close to the natural frequency of the harvester. The vortex shedding frequency is governed by the *Strouhal* number, S_t, of the flow, which is a dimensionless number that depends on the *Reynolds* number of the flow and the shape of the obstacle. Several studies have been carried out to investigate energy harvesting by adopting the wake-galloping mechanism [28, 29, 30].

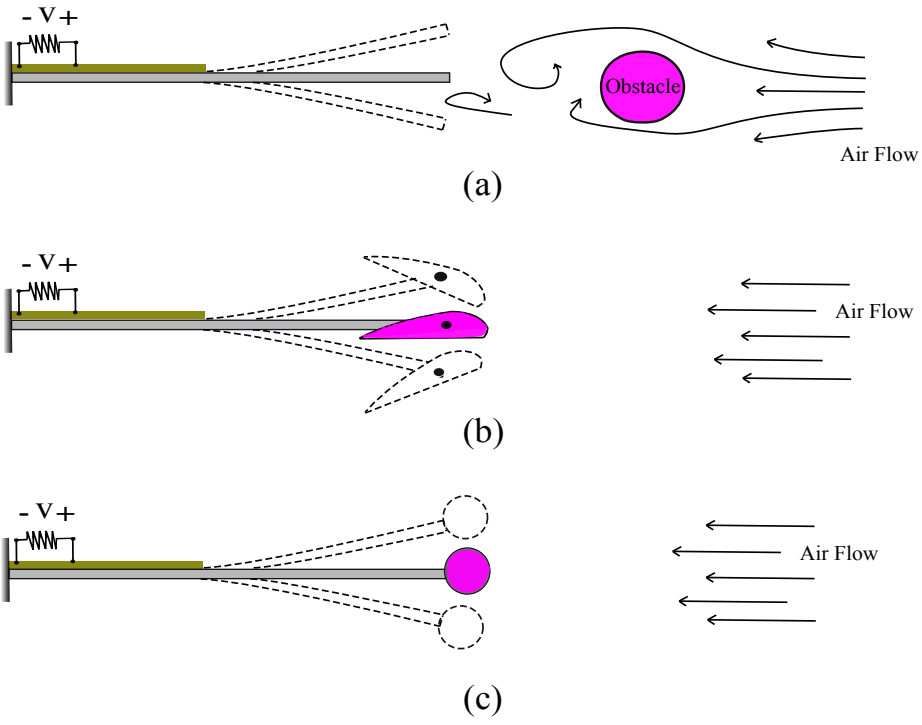

Figure 1.3: Flow energy harvesting mechanisms: (a) wake-galloping, (b) flutter (c) galloping instability.

A two-degree-of-freedom instability, known as flutter, has also been employed for flow energy harvesting. This approach makes use of an airfoil attached to the end of an elastic beam and allowed to pitch around an axis. When air flows past the airfoil, lift and moment forces are generated on the airfoil body. This causes the beam to oscillate with an amplitude which increases with the flow speed. This approach has also been used for flow energy harvesting [31, 32, 33, 34, 35].

Structural galloping, or the galloping instability, represents one of the most common types of fluid-structural coupling mechanisms used in flow energy harvesting [36, 37, 38, 39, 40]. As shown in Fig. 1.4, this dynamic instability is activated by the formation of inner circulation flow under that two shear layers that form as the fluid moves past an oscillator's bluff body. The circulation produces a negative surface pressure which causes a net lift on the body. The net lift breaks the symmetry between the shear layers on the top and bottom surfaces of the body which produces more lift. The process continues until the energy fed to the structure by the fluid balances the energy dissipated by the structures as it displaces the adjacent fluid. This results in a steady-state fixed-amplitude periodic motions known as limit-cycle oscillations. For such steady-state self-sustained oscillations to occur, the velocity of the fluid past the oscillator must exceed a certain threshold known as the cut-in flow speed which represents a projection of Hopf bifurcation in the amplitude versus flow velocity parameter's space.

1.2.1 Galloping Flow Energy Harvesters (GFEHs)

Galloping flow energy harvesters are suitable for harvesting energy from steady uniform flow patterns. Their efficacy and performance are characterized by two critical parameters: the cut-in flow speed which must be minimized and the output power which must be maximized. For a galloping energy harvester with a given bluff body, these two important quantities are generally controlled by the damping forces,

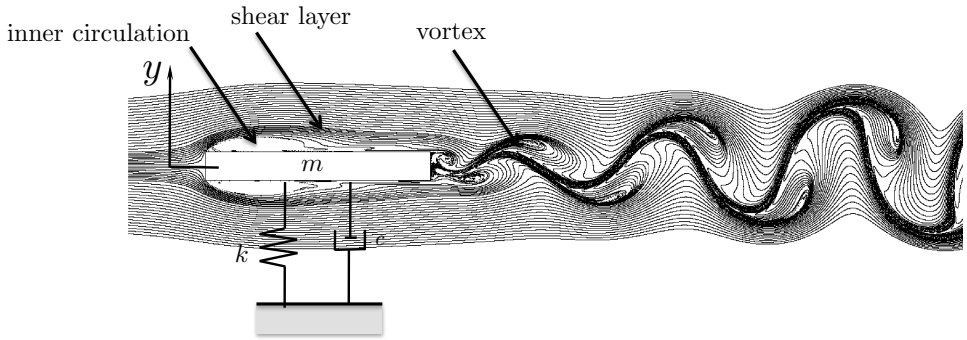

Figure 1.4: The inner circulation responsible for galloping.

the nature of the restoring force, and the electromechanical coupling. Since, for a given transduction mechanism, the magnitude of the electromechanical coupling is fixed while the intrinsic damping forces are generally beyond a designer's control, the restoring force of the oscillator is the main design parameter which can be used to control the efficiency of the harvester.

In the open literature, the restoring force of GFEHs has been considered to be linear [41, 29, 42, 43]. In this work, we consider the design of a GFEH with a nonlinear restoring force and study the influence of the nonlinearity on its performance. This approach has been utilized to enhance the bandwidth of vibratory energy harvesters but has never been investigated for FEHs [44, 22].

The three most common nonlinear restoring force elements are shown in Fig. 1.5. In the first, also known as a mono-stable hardening restoring force, the force required to achieve a unit deflection increases as the deflection of the oscillator increases. In the second type, known as a softening restoring force, the force required to achieve a unit deflection decreases as the deflection of the oscillator increases. Finally, the third type has a negative slope for small deflections and a positive slope for larger deflections resulting in a bi-stable response behavior. While the force-deflection relationship can be described by different functions, the most commonly adopted in the literature is cubic in nature and is widely known as the *Duffing* restoring

function. In such a scenario, the potential energy function of the oscillator is quartic in nature.

1.2.2 Wake-Galloping Flow Energy Harvesters

Wake galloping FEHs are suitable for harvesting energy from non-uniform flow conditions which can periodic, quasi-periodic, or even turbulent. Typically as shown earlier in Fig. 1.3 (a), a wake-galloping FEH consists of a mechanical oscillator coupled to an energy harvesting circuit through an electromechanical transduction element which can either be piezoelectric, electromagnetic, electrostatic, or magnetostrictive. The oscillator is placed in the downstream of a bluff body or an obstacle. When an initially steady fluid flows over the obstacle, it may undergo symmetry breaking in the form of a Von Kármán vortex street shedding from the trailing edge of the obstacle. The range of flow velocities for which a periodic Von Kármán vortex street can be initiated depends on the *Reynolds* number of the flow. For circular cylinders and very small *Reynolds* numbers, $Re \lesssim 40$, the shear layer does not have enough energy to detach from the trailing edge and the vortices remain confined to a recirculation bubble adjacent to the obstacle walls. However, as the *Reynolds* number is increased beyond $Re \approx 40$, the shear layer detaches from

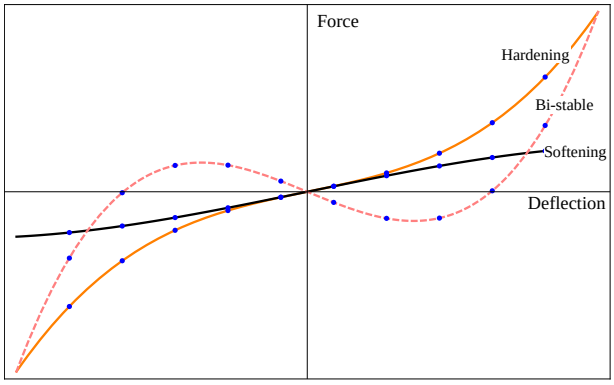

Figure 1.5: Different types of nonlinear restoring force elements used in energy harvesting.

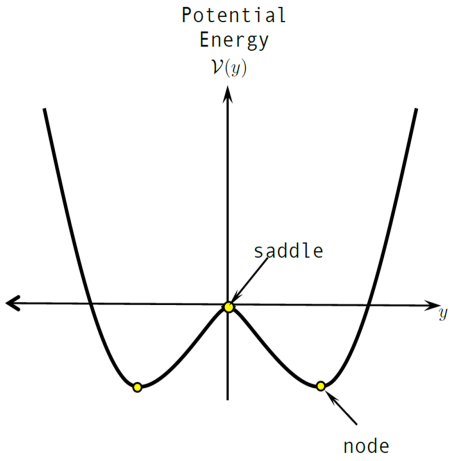

Figure 1.6: The associated potential energy function of the bi-stable system.

the obstacle and periodic vortex shedding occurs as a result of a Hopf bifurcation. A fast Fourier transform of the time series of the resulting flow velocity reveals a dominant frequency up to approximately $Re \approx 10^5$ [45]. Beyond this value of the *Reynolds* number quasi-periodic and chaotic flow patterns can be observed.

For the wide range of Re numbers where the vortex shedding is periodic, the shed vortices induce a periodic lift on the mechanical oscillator placed in the downstream of the bluff body. In the *lock-in* region where the vortex-shedding frequency is close to the natural frequency of the oscillator, the flow couples to the natural mode of the harvester resulting in large-amplitude motions. This results in kinetic energy transfer from the flow to the oscillator, which can be transformed into electricity using the electromechanical transduction element.

Wake-galloping FEHs have their own shortcomings. Typically, a wake-galloping FEH has a linear restoring force [30, 46], which results in a very narrow *lock-in* region. As a result, they do not respond well to the broad range of shedding frequencies normally associated with a variable flow speed. To enhance their response bandwidth under varying flow speeds, we propose exploiting stiffness nonlinearities in the

form of a bi-stable restoring force. As shown in Fig. 1.6, a bi-stable potential energy function consists of two potential wells (stable nodes) separated by a potential barrier (unstable saddle). Consequently, when the harvester interacts with the vortical structures generated by the obstacle, it can either perform small-amplitude resonant motions within a single potential well (intra-well motion); or large-amplitude non-resonant motions between the two potential wells (inter-well motion). It is widely accepted that the inter-well dynamics allow a harmonic oscillator to couple to the excitation over a wider range of frequencies [47].

This same concept has been used to improve the efficacy of vibratory energy harvesters (VEHs) [44, 48, 49]. Previous research findings indicated that, a carefully-designed nonlinear vibratory energy harvester has a wider steady-state bandwidth as compared to an equivalent linear device [50, 51, 52, 19]. Furthermore, a comparative uncertainty propagation analysis performed on linear and nonlinear VEHs indicated that the linear device is much more sensitive to uncertainties arising from imprecise characterization of the host environment and/or from manufacturing tolerances [53]. Such promising findings formed the basis of the work presented in this Dissertation.

Bi-stability may also be used to improve performance under multi-frequency periodic, quasi-periodic, or even fully turbulent flow conditions. This study aims to fill a void in the open literature by addressing this important issue. Since turbulence represents a flow regime characterized by rapid variations in pressure and velocity, it generates an excitation with wide-band frequency characteristics. Indeed, the more developed a turbulent flow is, the wider the frequency range over which its energy is distributed. As such, a harvester with a linear restoring force which has a very narrow frequency bandwidth is not expected to respond well to the broad range of frequencies associated with a turbulent flow. Therefore, in an attempt to enhance the response of a wake-galloping harvester in a turbulent regime, we hypothesize that it should be designed to have a bi-stable restoring force such that it couples to

the excitation over a wider range of frequencies.

1.3 Comparative Performance Analysis

As aforementioned, galloping FEH is suitable for uniform flow conditions while wake-galloping is better for periodic and aperiodic flow patterns. From a performance perspective, the attachment of the airfoil or prismatic structure to the flexible structure as in the flutter and galloping approaches increases the aeroelastic coupling due to the fact that the dynamic loads on the tip body are transmitted directly to the beam. This improves the fluid-elastic conversion efficiency by two-orders-of-magnitude when compared to the wake-galloping oscillations as reported in [54]. Additionally, for flutter and galloping-based harvesters, the onset of instability which results in steady-state oscillations is a consequence of a dynamic bifurcation, and is hence, followed by a monotonic increase in the output power with the wind speed. On the other hand, wake-galloping oscillators respond to the flow due to resonant interactions between the beam and the vortex shedding from the trailing edge of the bluff body. As such, large amplitude oscillations are only attainable for a small frequency bandwidth around the natural frequency of the beam. Those oscillations are also of the same order-of-magnitude as the characteristic length of the bluff body [54].

While no previous comparative studies have been performed, its the authors' opinion that, galloping is more suitable for energy harvesting than flutter because galloping-based harvesters are not sensitive to the coupling between the pitch and plunge modes which can shift the flutter speed into much higher wind velocities or lead to static divergence. Not to mention that, in the case of piezoelectric transduction, torsional mode oscillations of a flutter-based device cannot be easily captured and converted into electricity. It is also worth mentioning that depending on the size and

the shape of the prismatic body and the associated *Strouhal* number, a harvester may experience wake-galloping and galloping oscillations separately or in combination.

1.4 Objectives

The objective of this dissertation is three fold. First, it assesses the influence of stiffness nonlinearities on the performance of galloping FEHs under steady and laminar flow conditions. Second, it studies the influence of the nonlinearity on the response of a wake-galloping FEH to single- and multi-frequency Von Kármán vortex streets. Third, for known flow characteristics, the dissertation provides directions for how to choose the restoring force of the harvester to maximize the output power.

The contributions towards accomplishing the main objective of this thesis can be outlined as follows:

- **Investigate the influence of stiffness nonlinearity on the performance of GFEHs in a steady uniform flow**. To achieve this goal, a galloping based energy harvester which consists of a thin cantilever beam with a piezoelectric patch attached is considered. A square-sectioned bluff body is augmented at the free end of the beam to activate the galloping instability similar to the scheme shown in Fig. 1.3 (c). Two magnets located near the tip of the bluff body are used to introduce the nonlinearity which strength and nature can be altered by changing the distance between the magnets. Three nonlinear restoring forces are considered : bi-stable, mono-stable hardening, and mono-stable softening. A physics-based lumped-parameter aero-electromechanical model adopting the quasi-steady assumption for aerodynamic loading is presented and utilized to numerically simulate the harvester's response. The model is validated experimentally using wind tunnel tests performed under different wind speeds.

To explore the role of the main design parameters on the performance of the nonlinear GFEH, this dissertation obtains an approximate analytical solution of the derived lumped-parameters model. To achieve this task, a closed-form solution of the nonlinear response is obtained by employing a multiple-scaling perturbation analysis using the Jacobi elliptic functions. The attained solution is subsequently used to investigate the influence of the nonlinearity on the performance of the harvester and to illustrate how to optimize the restoring force in order to maximize the output power for given design conditions and airflow parameters.

- **Investigate the influence of a bi-stable restoring force on the performance of wake-galloping FEHs under single-frequency (periodic) vortex street**. The structure of this task is very similar to the first task with the main distinction that the harvester's performance is examined under periodic excitations. To generate the periodic vortex street, a square cylinder is placed in the windward direction of the harvester. A physics based electro-mechanical model is obtained by adopting the common uncoupled single-frequency force model. Numerical simulations are conducted to validate the model for different wind speeds. An approximate closed-form analytical solution of the validated model is then obtained by utilizing the method of multiple scales. The response of the linear and the bi-stable harvesters to the resulting vortex street is then evaluated as a function of the wind speed. The solution is used to study the influence of the shape of the potential energy function on the performance of the bi-stable FEH.

- **Study the influence of a bi-stable restoring force on the performance of wake-galloping FEHs under a multi-frequency Von Kármán vortex street**. This task is similar to the previous one with the main distinction that the harvester is studied under multi-frequency excitations. To that end,

multi-frequency Von Kármán vortex street is generated in a wind tunnel using static-grid structures located in the upstream of the bluff body. Three different mesh screens with square bars are designed with different bar and mesh widths to control the *Reynolds* numbers and associated unsteadiness. A series of wind tunnel tests are then used to experimentally compare the response of the linear and bi-stable FEHs. Wind velocity time history signals are utilized to characterize and relate the nature of the flow to the harvester's motion in terms of deflection and output voltage.

1.5 Dissertation Outline

The rest of the manuscript is organized as follows: Chapter 2 presents a physics-based lumped-parameters model of the nonlinear GFEH and validates it experimentally for various wind speeds. Chapter 3 presents an approximate analytical solution of the model derived in Chapter 2. Numerical simulations of the system's governing equations are also presented to validate the obtained solution. Chapter 4 presents a relative performance analysis of GFEHs exploiting different restoring forces, and presents a guide for designing the shape of the potential energy function. Chapter 5 investigates the performance of wake-galloping FEH employing a bi-stable restoring force to a single-frequency periodic excitation. Chapter 6 investigates the performance of bi-stable wake-galloping FEH under multi-frequency excitations. Finally Chapter 7 presents the conclusions and directions for future work.

Chapter 2

Galloping Flow Energy Harvesters: Modeling and Experimental Validations

In this Chapter, we obtain a physics-based mathematical model which represents the dynamics of a galloping based flow energy harvester utilizing a nonlinear restoring force. The model is obtained assuming piezoelectric transduction mechanism and a quasi-steady aerodynamic flow field. The importance of this model is to fully understand and characterize the behavior of the harvester, and to explore the role of the design parameters on the harvested power. To achieve this goal, the model is first validated by carrying out series of experiments investigating the response of the harvesting employing various nonlinear restoring forces.

2.1 Modeling and Classification

Figure 5.1 depicts a schematic of a piezoelectric GFEH. The harvester is placed in a uniform air flow with mean flow speed, U. When the flow speed exceeds the onset speed of galloping, U_0, the harvester undergoes steady-state limit-cycle oscillations in the cross-flow direction, y. These oscillations strain the piezoelectric element, which in turn, generates a voltage, V, across an electric load, R. The effective mass of the bluff body and the supporting structure is represented by M; while C represents the linear damping coefficient. The restoring force of the harvester can be represented as the partial derivative of the potential energy function, $\mathcal{V}$ with respect to y. The ordinary differential equations governing the dynamics of this lumped system can be written as

$$M\ddot{y} + C\dot{y} + \frac{d\mathcal{V}}{dy} - \theta V = F_y, \tag{2.1a}$$

$$C_p\dot{V} + \frac{V}{R} + \theta\dot{y} = 0, \tag{2.1b}$$

where the dot represents a derivative with respect to time, θ is the electromechanical coupling coefficient, and C_p is the capacitance of the piezoelectric element. The vertical component of the aerodynamic force, F_y, acting on the bluff body is modeled using a quasi-steady assumption with a cubic polynomial approximation in $\frac{\dot{y}}{U}$ as reported by [55].

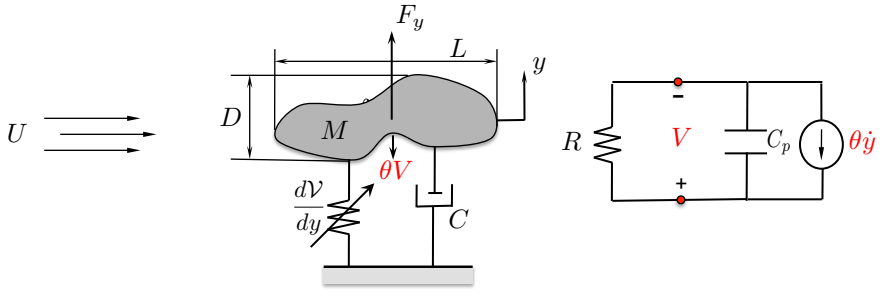

Figure 2.1: A schematic of a lumped-parameters model of a nonlinear galloping energy harvester.

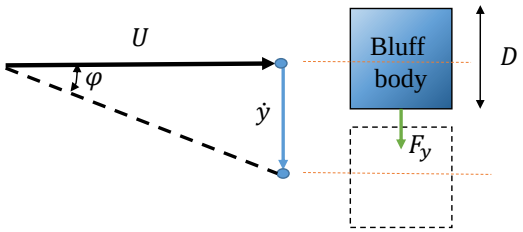

Figure 2.2: Tip bluff body in the presence of the flow.

In the quasi-steady assumption model the aerodynamic force, F_y, acting on the bluff body oscillating down with velocity, $\dot{y}$, in the presence of the wind velocity, U [56]. As depicted in Fig. 2.2, is assumed to be the same as the force on the bluff body at an angle of attack, φ, over a pertinent or applicable range. The aerodynamic force can be written as

$$F_y = \frac{1}{2} C_F \rho U^2 L D, \tag{2.2}$$

where ρ is the air density, L and D are, respectively, the length and the cross-flow dimension of the bluff body as shown in Fig. 5.1, C_F is the aerodynamic force coefficient represents the drag and left coefficient of forces applied to the bluff body in, y, direction and can expressed as a cubic function of the angle of attack, φ as

$$C_F = a_1 \varphi - a_3 \varphi^3. \tag{2.3}$$

The coefficients a_1 and a_3 account for the different geometries and aspect ratios of the bluff body. They are usually obtained empirically from normal aerodynamic force measurements on a static bluff body at different angles of attack [55], and the angle, φ, can be approximated for a small range of angle of attack as

$$\varphi \approx tan\varphi = \frac{\dot{y}}{U}. \tag{2.4}$$

Substituting Equation (2.4) into Equation (2.3) we get:

$$C_F = a_1 \frac{\dot{y}}{U} - a_3 \left(\frac{\dot{y}}{U} \right)^3. \tag{2.5}$$

Therefore, the aerodynamic force can be written as :

$$F_y = \frac{1}{2} \rho U^2 L D \left[a_1 \frac{\dot{y}}{U} - a_3 \left(\frac{\dot{y}}{U} \right)^3 \right]. \tag{2.6}$$

The total conservative energy of the harvester $\mathcal{E}$ can be written as the sum of the kinetic energy $\mathcal{T} = \frac{1}{2} M \dot{y}^2$ and the potential energy $\mathcal{V}$. While the potential energy function can take different forms, in this study we only consider the most common Duffing quartic potential which takes the form $\mathcal{V} = \frac{1}{2}\mu y^2 + \frac{1}{4}\gamma y^4$. Here, it is assumed that the potential function accounts for both the inherent stiffness in the system and the change in stiffness introduced through external force such as that resulting from magnetic interaction or pre-loading. Hence, the effective linear stiffness can be written as $\mu = \mu_i + \mu_e$, while the effective cubic stiffness is given by $\gamma = \gamma_i + \gamma_e$, where the subscripts 'i' and 'e' represent the inherent and the external components, respectively. The shape of the potential energy function of the system depends on the sign and magnitude of μ and γ. As depicted in Fig. 2.3, the potential function can be classified as follows:

1. Case (i) Hardening: Both μ and γ are positive. In this case, the potential function has a single minimum at $y_0 = 0$. Dynamic trajectories are always confined to one potential well, regardless of the kinetic energy of the system.

2. Case (ii) Softening: $\mu > 0$ and $\gamma < 0$. In this case, the potential function has two maxima (unstable saddles) at $y_0 = \pm\sqrt{\left|\frac{\mu}{\gamma}\right|}$ separated by a single minimum at $y_0 = 0$. The value of the potential energy at the maxima is given by $\mathcal{V}^* = \frac{\mu^2}{4|\gamma|}$. In the absence of damping and external forces, dynamic trajectories remain confined to the potential well when $\mathcal{E} \leq \mathcal{V}^*$ and will escape resulting in an unstable response otherwise.

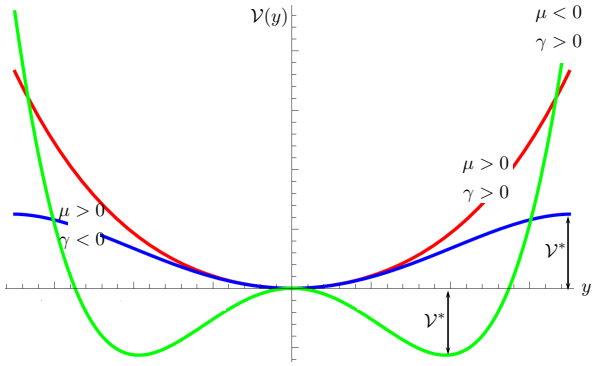

Figure 2.3: Different potential functions associated with nonlinear harvesters.

3. Case (iii) Bi-stable: $\mu < 0$ and $\gamma > 0$. In this case, the potential function has two minima (stable nodes) at $y_0 = \pm\sqrt{\left|\frac{\mu}{\gamma}\right|}$ separated by a single maximum at $y_0 = 0$. The value of the potential energy at the minima is given by $\mathcal{V}^* = -\frac{\mu^2}{4|\gamma|}$. In the absence of external forces, dynamic trajectories remain confined to a single potential well (intra-well oscillations) when $\mathcal{E} \leq 0$, Case (iii) (a). Otherwise, the dynamic trajectories escape the single potential well resulting in cross-well or inter-well motions, Case (iii) (b).

4. Case (iv) Unstable: $\mu < 0$ and $\gamma < 0$. In this case, the potential function has a single maximum (unstable node) at $y_0 = 0$. Any perturbations around the equilibrium point will result in an unstable response. This extreme case will not be considered in this analysis.

With these definitions, the final equations of motion can be written as

$$M\ddot{y} + C\dot{y} + \mu y + \gamma y^3 - \theta V = \frac{1}{2}\rho U^2 LD\left[a_1\frac{\dot{y}}{U} - a_3\left(\frac{\dot{y}}{U}\right)^3\right], \tag{2.7a}$$

$$C_p\dot{V} + \frac{V}{R} + \theta\dot{y} = 0. \tag{2.7b}$$

2.2 Experimental Validations

Here, we investigate whether the model presented in this chapter can, at least, qualitatively capture the dynamics of a GFEH with different types of restoring force. To that end, we develop an experimental setup following the schematic shown in Fig. 2.4. We consider a galloping piezoelectric FEH which consists of a metallic cantilever beam fixed at one end and free to oscillate at the other. A square-sectioned bluff body is attached to the free end and is perpendicular to the direction of the flow.

The harvester makes use of different configurations of repulsive and attractive magnets to change and control the nature of the restoring force. The bi-stable configuration is created by using two repulsive magnets, A, and, B, placed at a distance h. The mono-stable hardening and softening configurations are produced by removing magnet, B, and using magnets A, C, and D, instead. The hardening case makes use of repulsive forces between the moving magnet A, and the fixed magnets C and D; while in the softening case, the polarity of the two magnets, C, and D, is reversed creating attractive forces towards magnet A.

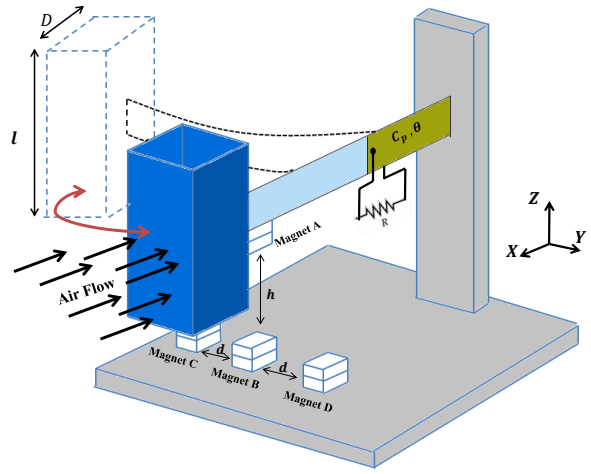

Figure 2.4: A schematic diagram of the galloping nonlinear FEH.

A series of wind tunnel experiments are conducted using the experimental setup depicted in Fig. 6.2. The wind tunnel is equipped with an air velocity tuner having a speed resolution as of 0.1 m/s. A digital anemometer is used to measure the air velocity, and a laser vibrometer is used to record the tip displacement. The stainless beam has dimensions of $209 \times 24 \times 1$ mm^3, while the piezoelectric layer has dimensions of $95 \times 28 \times 0.2$ mm^3. A square-sectioned bluff body with dimensions of $50 \times 50 \times 100$ mm^3 is attached to the free end of the cantilever beam and faces the flow direction. A resistor box is used to vary the resistive load, R, which is connected in parallel to the piezoelectric patch.

2.2.1 Response of the linear system

The behavior of the linear system (without magnets) is first investigated in order to identify system parameters. The natural frequency at short-circuit conditions was experimentally identified as $\omega_n = 3.60$ Hz. The mechanical damping ratio ζ_m of the system was estimated experimentally using the logarithmic decrement method and

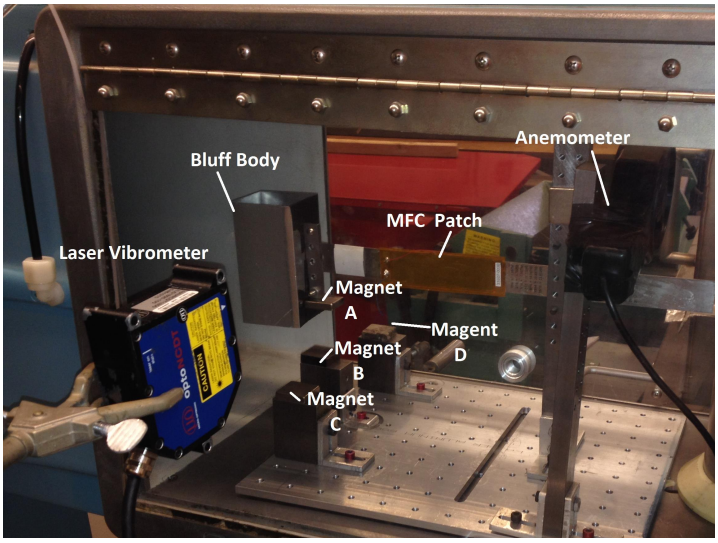

Figure 2.5: Overview of the experimental setup.

averaged at $\zeta_m = 0.003$ for three experimental runs. The aerodynamics constants a_1 and a_3 were also obtained experimentally as $a_1 = 2.5$ and $a_3 = 130$ using the relation between the tip displacement and wind velocity [57].

The effective capacitance of the piezoelectric layer C_p and electromechanical coupling θ were determined experimentally by performing a resistive load sweep at a constant wind speed of 7 m/s and measuring the power harvested at each resistance as illustrated in Fig. 2.6. The optimal power, P_{opt}, and the effective capacitance, C_p, can be written as

$$P_{opt} = \frac{V^2}{R_{opt}}, \tag{2.8}$$

$$C_p = \frac{1}{R_{opt}\ \omega_n}. \tag{2.9}$$

From the resistive load sweep experiment we estimated the optimal resistance at which the harvester generates the maximum power, and by using Equation. (2.9)

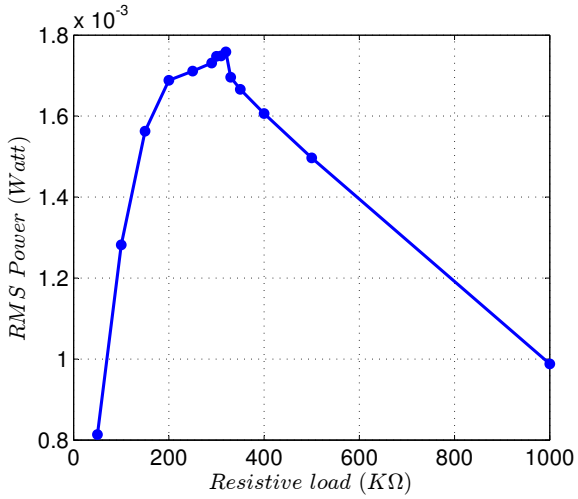

Figure 2.6: A resistive load sweep to determine the optimal resistance.

the effective capacitance is found to be 187 nF and the electromechanical coupling coefficient, θ, is 1.9×10^{-4} N/V. The geometric and material properties of the system are further listed in Table 2.1.

Table 2.1: Material and geometric properties of the harvester.

Parameter (symbol)	Value
Cantilever beam length	0.209 m
Effective mass (M)	0.1134 Kg
Damping ratio (ζ)	0.003
Air Density (ρ)	1.24 Kg/m^3
Capacitance of the MFC patch (C_p)	187 nF
Electromechanical coupling (θ)	1.9×10^{-4} N/V
Bluff body height (L)	0.1 m
Cross flow dimension (D)	0.05 m
Linear aerodynamic coefficient (a_1)	2.5
Cubic aerodynamic coefficient (a_3)	130

2.2.2 Response of mono-stable hardening and softening systems

Figure 2.7 depicts a comparison between the numerical simulations obtained using the experimentally identified parameters and the experimental measurements for both of the steady-state tip deflection response and output voltage across a constant resistive load of 270 KΩ. Results are shown for the linear, hardening, and softening

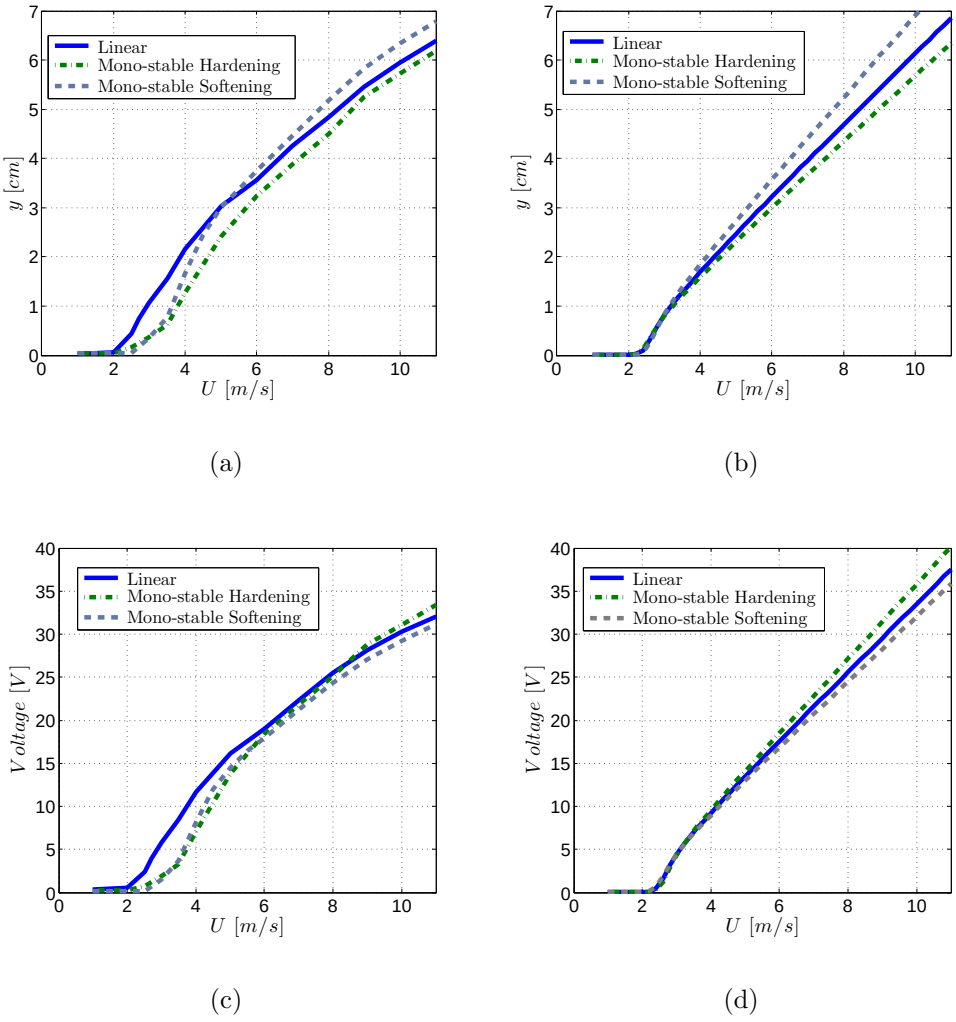

Figure 2.7: Beam's tip deflection and the associated output voltage measured at a resistive load, R=270 KΩ. Results are obtained for the linear case, softening, and hardening restoring force systems. (a)&(c) Experimental results (b)&(d) numerical simulations.

springs.

First, it is evident that there is a good qualitative agreement between the numerical simulations and the experimental data. Second, one can clearly see that the cut-in wind speed which represents a Hopf bifurcation in the deflection/voltage versus wind velocity parameters' space does not change appreciably for the different configurations. This stems from the fact that the Hopf bifurcation point is governed

by the linear parameters only. These parameters do not change significantly for the three different configurations. Finally, it can also be noted that the steady-state deflection associated with the softening spring is larger than that associated with the linear and hardening springs for the same wind speed. This is expected since the softening spring will exert less force while resisting the lift force especially away from the Hopf bifurcation point. On the other hand, a reverse trend can be observed when inspecting the steady-state voltage. Here, the hardening spring outperforms the linear and softening springs. This can be explained by understanding that the voltage is proportional to the velocity of the oscillator which increases with the frequency of oscillation. Therefore, since the hardening spring generally has a higher response frequency, it produces higher voltage levels.

2.2.3 Response of the bi-stable system

A similar comparison, but with two different bi-stable restoring forces replacing the softening and hardening springs, is presented in Fig. 2.8. Again the results are obtained for a fixed load resistance of 270 KΩ. Due to the bi-stability, the harvester can either perform small intra-well oscillations within one potential well or large amplitude inter-well motions. This is also evident in the bifurcation diagrams where, in both scenarios, the harvester performs small-amplitude intra-well motions followed by a sudden jump to a larger inter-well periodic orbit. As expected, the jump occurs at higher wind speeds for the harvester possessing deeper potential wells. Also, it should be noted that, due to the presence of multiple coexisting stable solutions, a hysteretic behavior can occur as the jump from intra- to inter-well motions occurs at higher wind speed in a forward velocity sweep, see window in Fig. 2.8 (a).

A comparison among the steady-state deflections in the three scenarios reveals that the linear FEH undergoes larger deflections near the lower end of wind speeds while

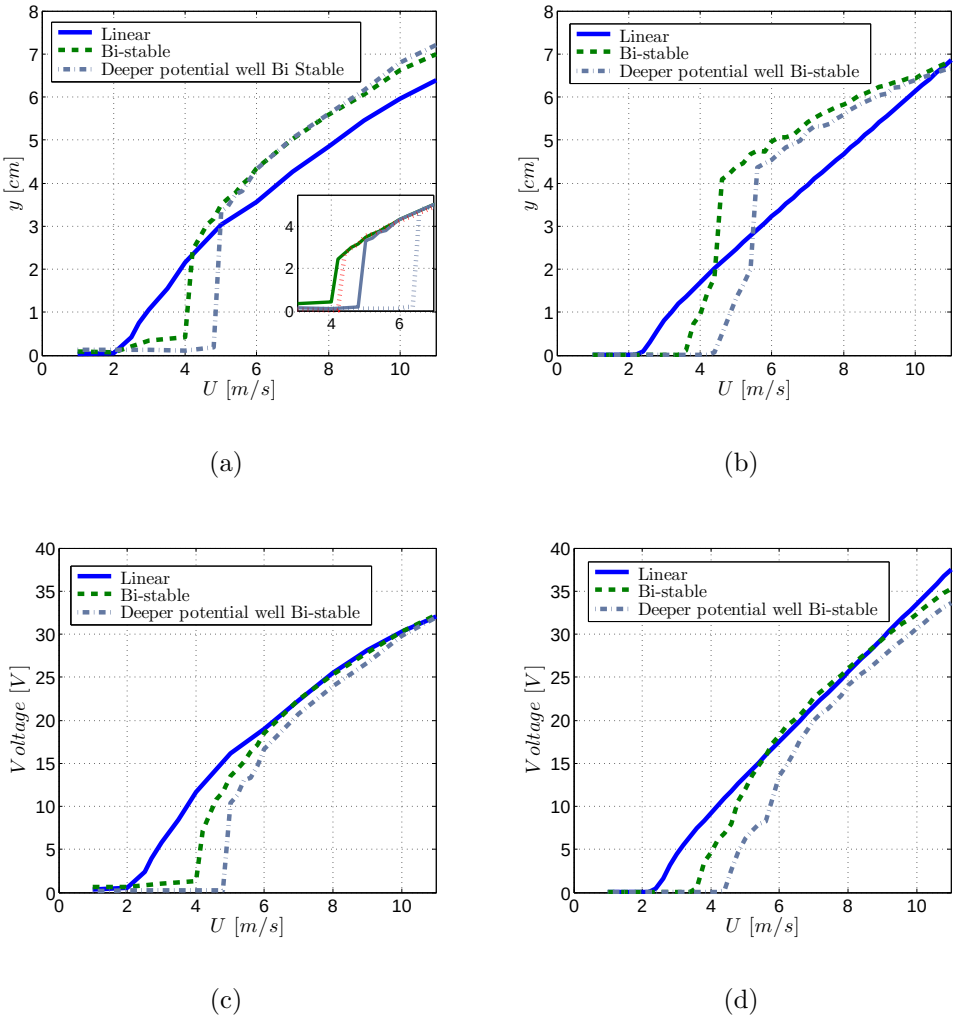

Figure 2.8: Beam's tip deflection and the associated output voltage measured at a resistive load, R=270 KΩ. Results are obtained for the linear and bi-stable cases. (a)&(c) Experimental results (b)&(d) numerical simulations.

the bi-stable harvesters undergo larger deflections when the wind speed is large enough to allow the dynamic trajectories to escape form a single potential well. However, these trends are not reflected in the voltage response as the linear harvester clearly outperforms the bi-stable designs over the whole range of wind speeds.

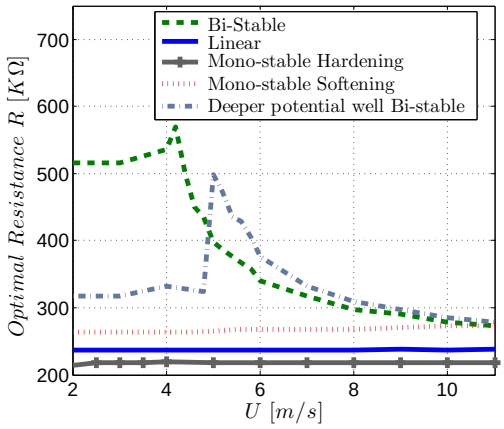

Figure 2.9: Variation of the optimal resistance with the wind speed.

2.2.4 Optimal power

For a fair performance comparison among all configurations, the harvested power was experimentally obtained at the optimal load for each wind speed. As shown in Fig. 2.9, the optimal load which is a function of the oscillation frequency is clearly dependent on the wind speed especially for the nonlinear bi-stable harvesters.

Figure 2.10 illustrates this comparison for the four different configurations considered. It is clearly evident that a GFEH with a nonlinear hardening restoring force outperforms all other configurations especially for the higher range of wind speeds. This configuration produces approximately 21% more power than the optimized linear device at a wind speed of 10 m/s.

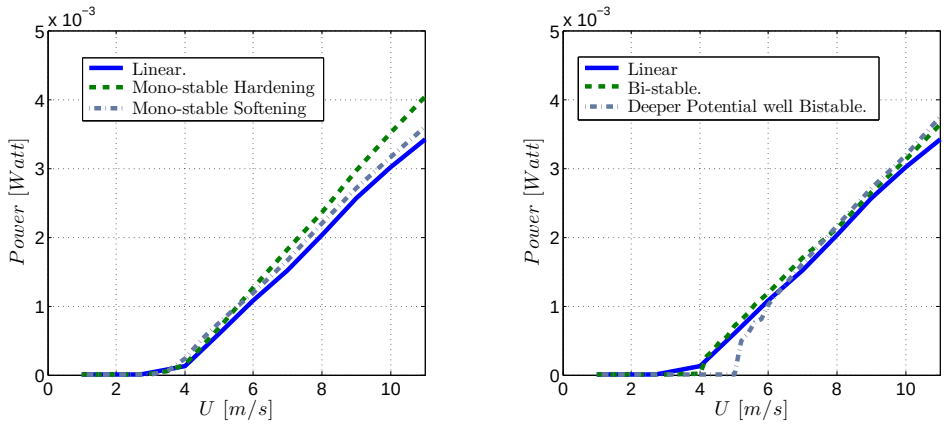

(a) (b)

Figure 2.10: Optimal power curves for (a) linear, mono-stable hardening, and mono-stable softening restoring forces and, (b) linear and bi-stable restoring forces.

Chapter 3

Perturbation Anaylsis: Approximate Analytical Soultion

In this Chapter, we present a nonlinear analysis for the lumped-parameters model discussed in Chapter 2. The main objective of this analysis is to gain a better qualitative understanding of the role of the design parameters on the performance of the energy harvester. To achieve this goal, a non-dimensional model is first presented. The method of multiple scales utilizing Jacobi elliptic functions is then used to obtain an approximate analytical solution of the asymptotic response. Finally, the approximate analytical solution is numerically validated and compared to a numerical integration of the governing equations.

3.1 Non-dimensional Model

To obtain a dimensionless form of Equations (2.7a) and (2.7b), we introduce the following non-dimensional parameters

$$\bar{y} = \frac{y}{D}, \quad \bar{V} = \frac{C_p}{\theta D} V, \quad \bar{m} = \frac{\rho L D^2}{4M}, \quad \bar{U} = \frac{U}{\omega_n D}, \quad \kappa = \frac{\theta^2}{M\omega_n^2 C_p}, \quad \alpha = \frac{1}{RC_p\omega_n},$$

where $\bar{y}$ and $\bar{V}$ represent the dimensionless transverse displacement and voltage respectively, $\bar{m}$ is the flow to harvester mass ratio, $\bar{U}$ is the reduced wind speed, κ is the dimensionless electromechanical coupling, α is the mechanical to electrical time-constant ratio. The natural frequency of the harvester at short-circuit conditions is given by $\omega_n = \sqrt{\mu_i/M}$ and used to introduce the non-dimensional time as $\bar{t} = \omega_n t$; whereas the mechanical damping ratio ζ_m is defined by $C = 2\zeta_m M\omega_n$. Equations (5.1a) and (5.1b) can be expressed in terms of the non-dimensional parameters as

$$\bar{y}'' + \zeta_1\bar{y}' + \zeta_3\bar{y}'^3 + \bar{\mu}\bar{y} + \bar{\gamma}\bar{y}^3 - \kappa\bar{V} = 0, \tag{3.1a}$$

$$\bar{V}' + \alpha\bar{V} + \bar{y}' = 0, \tag{3.1b}$$

where the prime denotes a derivative with respect to the non-dimensional time $\bar{t}$, and

$$\zeta_1 = 2\left[\zeta_m - \bar{m}a_1\bar{U}\right], \quad \zeta_3 = \frac{2\bar{m}a_3}{\bar{U}}, \quad \bar{\mu} = 1 + \frac{\mu_e}{\mu_i} \quad , \quad \bar{\gamma} = \frac{\gamma D^2}{\mu_i}.$$

3.2 Jacobi Elliptic Functions

The easiest way to understand the Jacobi elliptic functions is to cast them in terms of the solution of the following third-order nonlinear system:

$$\dot{x} = yz, \qquad \dot{y} = -zx, \qquad \dot{z} = -m^2xy \tag{3.2}$$

subjected to the initial condition $x(0) = 0$, $y(0) = 1$, $z(0) = 1$. Equation (3.2) admits a periodic, real, analytic solution of the form:

$$\begin{aligned} x(t) &= \mathrm{sn}(t, m), \\ y(t) &= \mathrm{cn}(t, m), \\ z(t) &= \mathrm{dn}(t, m), \end{aligned} \tag{3.3}$$

where $0 < m < 1$ is known as the modulus, $\mathrm{sn}(t, m)$ is known as the sine elliptic function, $\mathrm{cn}(t, m)$ is known as the cosine elliptic function, and $\mathrm{dn}(t, m)$ is known

as the delta elliptic function. It follows from Equations (3.2) and (3.3) that the derivatives of the Jacobi elliptic functions can be written as

$$\begin{aligned}
\frac{d}{dt}\mathrm{sn}(t,m) &= \mathrm{cn}(t,m)\mathrm{dn}(t,m),\\
\frac{d}{dt}\mathrm{cn}(t,m) &= -\mathrm{sn}(t,m)\mathrm{dn}(t,m),\\
\frac{d}{dt}\mathrm{dn}(t,m) &= -m^2\mathrm{cn}(t,m)\mathrm{sn}(t,m).
\end{aligned} \tag{3.4}$$

It can be easily proven that the Jacobi elliptic functions satisfy the following equalities:

$$\begin{aligned}
x^2 + y^2 &= 1,\\
m^2x^2 + z^2 &= 1.
\end{aligned} \tag{3.5}$$

For instance, if we differentiate the first equality we get $2x\dot{x} + 2y\dot{y} = 0$, and by virtue of Equation (3.2), $2x(yz) + 2y(-zx) = 0$. Equation (3.5) yields the following identities

$$\begin{aligned}
\mathrm{sn}^2(t,m) + \mathrm{cn}^2(t,m) &= 1,\\
k^2\mathrm{sn}^2(t,m) + \mathrm{dn}^2(t,m) &= 1,
\end{aligned} \tag{3.6}$$

and the following important inequalities:

$$\begin{aligned}
-1 \leq \mathrm{sn}(t,m) &\leq 1,\\
-1 \leq \mathrm{cn}(t,m) &\leq 1,\\
\sqrt{1-m^2} \leq \mathrm{dn}(t,m) &\leq 1.
\end{aligned} \tag{3.7}$$

Furthermore, since the Jacobi elliptic functions satisfy Equation (3.5), it can be conclude that the solution $(x(t), y(t), z(t)) \equiv (\mathrm{sn}(t,m), \mathrm{cn}(t,m), \mathrm{dn}(t,m))$ is a closed loop formed by the intersection of the two surfaces represented by Equation (3.5). This closed loop contains no equilibria, and hence, represents a periodic solution. Using some mathematical manipulations, one can show that the period of these oscillations can be related to the following integral known as the complete elliptic integral of the first kind:

$$K_J = \int_0^{\pi/2} \frac{d\theta}{\sqrt{1 - m^2\sin^2\theta}}. \tag{3.8}$$

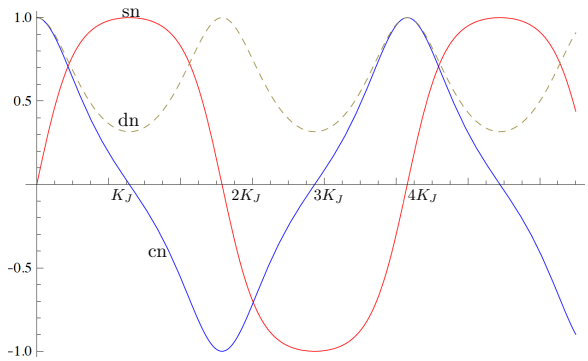

Figure 3.1: The functions $\mathrm{sn}(t,m), \mathrm{cn}(t,m), \mathrm{dn}(t,m)$ for $m = 0.9$.

Figure 3.1 depicts a the Jacobi elliptic functions for $m = 0.9$. As can be seen in the figure, $\mathrm{sn}(t,m)$, and $\mathrm{cn}(t,m)$ has a period of $4K_J$ while $\mathrm{dn}(t,m)$ has a period of $2K_J$. Another important complete elliptic integral is that of the second kind and is given by:

$$E_J = \int_0^{\pi/2} \sqrt{1 - m^2 \sin^2\theta} d\theta. \tag{3.9}$$

This integral is related to the length of the closed loop formed by the loci of $(x(t), y(t), z(t))$.

3.3 Approximate Analytical Solution

In this section, we utilize the method of multiple scales [58] to obtain an approximate analytical solution of Equations (3.1a) and (3.1b). Towards that end, the time dependence is expanded into ordinary and slow time scales in the form $T_0 = \bar{t}$ and $T_1 = \epsilon\bar{t}$, respectively, where ϵ is a scaling parameter. The time derivatives can then

be expressed as

$$\begin{aligned} \frac{d}{d\bar{t}} &= D_0 + \epsilon D_1 + O(\epsilon^2), \\ \frac{d^2}{d\bar{t}^2} &= D_0^2 + 2\epsilon D_0 D_1 + O(\epsilon^2), \end{aligned} \tag{3.10}$$

where $D_n = \frac{\partial}{\partial T_n}$. Furthermore, the variables $\bar{y}$ and $\bar{V}$ are expanded in the following forms:

$$\begin{aligned} \bar{y}(\bar{t}) &= \bar{y}_0(T_0, T_1) + \epsilon \bar{y}_1(T_0, T_1) + O(\epsilon^2), \\ \bar{V}(\bar{t}) &= \bar{V}_0(T_0, T_1) + \epsilon \bar{V}_1(T_0, T_1) + O(\epsilon^2). \end{aligned} \tag{3.11}$$

The constant coefficients in Equation (3.1a) are also scaled such that the effects of damping and electromechanical coupling appear at the second order of the perturbation problem. In other words, we let

$$\zeta_1 = \epsilon\zeta_1, \qquad \zeta_3 = \epsilon\zeta_3, \qquad \kappa = \epsilon\kappa. \tag{3.12}$$

Note that the nonlinearity coefficient is not scaled at order ϵ, and, hence can be as large as order one. Next, the time scales, their derivatives, and the scaled parameters are substituted back into Equations (3.1a) and (3.1b). Collecting terms of equal powers of ϵ yields

$O(\epsilon^0)$:

$$D_0^2 \bar{y}_0 + \bar{\mu}\bar{y}_0 + \bar{\gamma}\bar{y}_0^3 = 0, \tag{3.13}$$

$$D_0 \bar{V}_0 + \alpha \bar{V}_0 = -D_0 \bar{y}_0, \tag{3.14}$$

$O(\epsilon^1)$:

$$D_0^2 \bar{y}_1 + \bar{\mu}\bar{y}_1 + 3\bar{\gamma}\bar{y}_0^2 \bar{y}_1 = -2D_0 D_1 \bar{y}_0 - \zeta_1 D_0 \bar{y}_0 - \zeta_3 \left(D_0 \bar{y}_0\right)^3 + \kappa \bar{V}_0, \tag{3.15}$$

$$D_0 \bar{V}_1 + \alpha \bar{V}_1 = -D_1 \bar{V}_0 - D_1 \bar{y}_0 - D_0 \bar{y}_1, \tag{3.16}$$

The solution of the zeroth-order perturbation problem, Equation (3.13), can be written in terms of Jaccobi elliptic functions as

$$\bar{y}_0 = A(T_1) \mathrm{Ep}\left(\psi, m\right), \tag{3.17}$$

where Ep is a general expression of the Jacobi elliptic sine (sn), cosine (cn), and delta (dn) functions. The parameters $A(T_1)$, $\psi = \omega T_0 + \phi(T_1)$, and m are respectively, the unknown amplitude, argument, and modulus of the Jacobi elliptic function. Here, ω is the frequency and ϕ is the phase angle of the response.

Depending on the shape of the potential energy function, three different cases can be distinguished:

- **Hardening Responses Case (i) and Case (iii) (b):**

  In this scenario, Equation (3.17) takes the form of a cosine elliptic function; that is

  $$\bar{y}_0 = A(T_1)\mathrm{cn}\left(\omega T_0 + \phi(T_1), m\right), \tag{3.18}$$

  where $0 < m < 1$. To first obtain the unknown frequency and modulus of the response, we substitute Equation (3.18) back into Equation (3.13); this yields

  $$\begin{aligned} \omega^2 &= \bar{\mu} + \bar{\gamma}A^2(T_1), \\ m &= \frac{\bar{\gamma}A^2(T_1)}{2\omega^2}. \end{aligned} \tag{3.19}$$

  The first-order approximation of the voltage can then be obtained by substituting the time derivative of Equation (3.18) into Equation (3.14); this yields

  $$D_0\bar{V}_0 + \alpha\bar{V}_0 = \omega A(T_1)\mathrm{sn}(\psi, m)\mathrm{dn}(\psi, m). \tag{3.20}$$

  Unfortunately, to the authors' knowledge, a closed form analytical solution of Equation (3.20) does not readily exist. Here, we propose to obtain an approximate solution by expanding the product $\mathrm{sn}(\psi, m)\mathrm{dn}(\psi, m)$ in terms of $\mathrm{sn}(\psi, m)$ using the best L_2 norm approximation as

  $$\mathrm{sn}(\psi, m)\mathrm{dn}(\psi, m) \approx \frac{\pi m}{4\left(K_J - E_J\right)}\mathrm{sn}(\psi, m), \tag{3.21}$$

where $K_J \equiv K_J(m)$ and $E_J \equiv E_J(m)$ are, respectively, the complete elliptic integrals of the first and the second kind. Another approximation is made by replacing $\mathrm{sn}(\psi, m)$ with the trigonometric sine function $\sin(\Omega T_0)$ such that they have the same oscillation frequency, i.e. $\Omega = \frac{2\pi\omega}{4K_J}$. These approximations are very reasonable as will be seen later in section 3.5.

Upon substituting the aforementioned approximations, the solution of Equation (3.20) can be written as

$$\bar{V}_0 = \frac{\pi m}{4\left(K_J - E_J\right)} \frac{\omega A(T_1)}{\sqrt{\Omega^2 + \alpha^2}} \sin\left(\Omega T_0 - \delta\right), \tag{3.22}$$

where $\delta = \sin^{-1}\left(\frac{\Omega}{\sqrt{\Omega^2+\alpha^2}}\right)$.

Next, we determine the unknown amplitude, $A(T_1)$, by substituting Equations (3.18) and (3.22) back into Equation (3.15), then eliminating the secular terms. Those terms can be identified by multiplying the right-hand side of Equation (3.15) by $\mathrm{sn}(\psi, m)\mathrm{dn}(\psi, m)$, then averaging over the period of the Jacobi elliptic functions, $4K_J$. This yields the following amplitude modulation equation:

$$D_1 A = -\frac{\zeta_T}{2} A - \frac{\zeta_3}{2} \omega^2 \Gamma_{\mathrm{cn}} A^3, \tag{3.23}$$

where $\zeta_T = \zeta_1 + \zeta_e$ is the effective damping, in which the electrical damping component is given by

$$\zeta_e = \frac{\kappa\alpha}{(\Omega^2 + \alpha^2)}, \tag{3.24}$$

and

$$\Gamma_{\mathrm{cn}} = \frac{35m}{3} \frac{\left[\left(-16m^3 + 24m^2 - 4m - 2\right) E_J + \left(8m^3 - 13m^2 + 3m + 2\right) K_J\right]}{\left[\left(2m - 1\right) E_J + \left(1 - m\right) K_J\right]}. \tag{3.25}$$

- **Softening Symmetric Responses Case (ii):**

In case (ii), the solution of the zeroth-order perturbation problem can be written in terms of the sine elliptic function as

$$\bar{y}_0 = A(T_1)\mathrm{sn}\left(\omega T_0 + \phi(T_1), m\right), \tag{3.26}$$

where the frequency of oscillation and the modulus are related to the amplitude via

$$\begin{aligned} \omega^2 = &\ \bar{\mu} + \frac{\bar{\gamma}}{2} A^2(T_1), \\ m = &\ \frac{-\bar{\gamma} A^2(T_1)}{2\omega^2}. \end{aligned} \tag{3.27}$$

Substituting Equation (3.26) into Equation (3.14) and approximating the product $\mathrm{cn}(\psi, m)\mathrm{dn}(\psi, m)$ in terms of the trigonometric cosine function as

$$\begin{aligned} \mathrm{cn}(\psi, m)\mathrm{dn}(\psi, m) \approx &\ \frac{\pi m}{4\left(E_J - (1-m)K_J\right)} \cos(\Omega T_0), \\ \Omega = &\ \frac{2\pi\omega}{4K_J}, \end{aligned} \tag{3.28}$$

we obtain the following expression for the dimensionless voltage

$$\begin{aligned} \bar{V}_0 = &\ \frac{\pi m}{4\left((1-m)K_J - E_J\right)} \frac{\omega A(T_1)}{\sqrt{\Omega^2 + \alpha^2}} \cos\left(\Omega T_0 - \delta\right), \\ \delta = &\ \sin^{-1}\left(\frac{\Omega}{\sqrt{\Omega^2 + \alpha^2}}\right). \end{aligned} \tag{3.29}$$

Slow modulation of the response amplitude, $A(T_1)$ can now be obtained by substituting Equation (3.26) and Equation (3.29) into the first-order perturbation problem, Equation (3.15), and eliminating the secular terms; this yields

$$D_1 A = -\frac{\zeta_T}{2} A - \omega^2 \frac{\zeta_3}{2} \Gamma_{\mathrm{sn}} A^3, \tag{3.30}$$

where the averaging coefficients are given by

$$\Gamma_{\mathrm{sn}} = \frac{35m}{3} \frac{\left[\left(2m^3 - 10m^2 - 10m + 2\right) E_J + \left(-m^3 - 8m^2 + 11m - 2\right) K_J\right]}{\left[(1+m) E_J - (1-m) K_J\right]}. \tag{3.31}$$

- **Softening Asymmetric Responses Case (iii):**

  For the intra-well motion, case (*iii*), i.e. softening asymmetric solutions, the solution of the zeroth-order perturbation takes the form of the delta elliptic function as follows:

$$\bar{y}_0 = A(T_1)\mathrm{dn}\left(\omega T_0 + \phi(T_1), m\right). \tag{3.32}$$

where the frequency and modulus are further related to the amplitude through

$$\begin{aligned} \omega^2 = & \frac{1}{2}\bar{\gamma}A^2(T_1), \\ m = & 2\left(1+\frac{\bar{\mu}}{\bar{\gamma}A^2(T_1)}\right). \end{aligned} \tag{3.33}$$

By inspecting Equations (3.33), one can correctly surmise that, when $0 < m < 1$, the amplitude of the intra-well oscillations satisfies $A^2 < \frac{-2\bar{\mu}}{\bar{\gamma}}$. As such, Equation (3.32) is only valid when $A^2 < \frac{-2\bar{\mu}}{\bar{\gamma}}$. Otherwise, bi-stable inter-well oscillations can be excited and one has to revert back to Equation (3.23). Upon substituting the derivative of Equation (3.32) in Equation (3.14) and approximating the product $\mathrm{sn}(\psi,m)\mathrm{cn}(\psi,m)$ in terms of equal-frequency trigonometric functions, i.e. $\sin(\Omega T_0)\cos(\Omega T_0)$ where $\Omega = \frac{2\pi\omega}{4K_J}$, we obtain the following dimensionless voltage equation:

$$\begin{aligned} \bar{V}_0 = & \frac{1}{2}\frac{m\omega A}{\sqrt{(2\Omega)^2+\alpha^2}}\sin\left(2\Omega T_0-\delta\right), \\ \delta = & \sin^{-1}\left(\frac{2\Omega}{\sqrt{(2\Omega)^2+\alpha^2}}\right). \end{aligned} \tag{3.34}$$

The amplitude modulation equation can be obtained by substituting Equation (3.32) and Equation (3.34) in the first-order perturbation problem, Equation (3.15), and eliminating the secular terms. To that end, the right-hand side of Equation (3.15) is multiplied by the product $\mathrm{sn}(\psi,m)\mathrm{cn}(\psi,m)$ and the resulting expression is averaged over the period $4K_J$ to obtain

$$D_1 A = -\frac{\zeta_T}{2}A - \frac{\zeta_3}{2}\omega^2\Gamma_{\mathrm{dn}}A^3, \tag{3.35}$$

where the averaging coefficients are given by

$$\Gamma_{\mathrm{dn}} = \frac{35m}{3}\frac{\left[\left(m^3+15m^2-32m+16\right)K_J-\left(2m^3+4m^2-24m-16\right)E_J\right]}{\left[2\left(m-1\right)K_J-\left(m-2\right)E_J\right]}. \tag{3.36}$$

It is worth noting that in all the cases analyzed the modulation equations take the same form with the only difference occurring in the resulting expression for Γ.

3.4 Asymptotic Response

To investigate the steady-state response, we set the time derivative in the modulation equation to zero, i.e. $D_1 A = 0$. This yields another algebraic equation that governs the frequency, modulus, and the steady-state amplitude of the non-trivial solution. Again, three cases can be distinguished here: for case (i) and case (iii) (b), the steady-state amplitude can be written as

$$A^2 = -\frac{\zeta_T}{\omega^2 \zeta_3 \Gamma_{\mathrm{cn}}}. \tag{3.37}$$

Rewriting Equations (3.19) in terms of the modulus m yields

$$\begin{aligned} \omega^2 &= \frac{\bar{\mu}}{(1-2m)}, \\ A^2 &= \frac{2\bar{\mu} m}{\bar{\gamma}\,(1-2m)}. \end{aligned} \tag{3.38}$$

By substituting Equations (3.38) into Equation (3.37), we eliminate the dependence on A and ω to obtain the following equation for the modulus of the elliptic function:

$$-\frac{\bar{\gamma}\zeta_T}{2\bar{\mu}^2\zeta_3} = \frac{m\Gamma_{\mathrm{cn}}}{(1-2m)^2} = f_{\mathrm{cn}}(m). \tag{3.39}$$

Equation (3.39) represents the response equation in terms of the modulus and the other design parameters. The left-hand side contains the nonlinearity factor $\bar{\gamma}$ and the other design parameters including the wind speed. The right-hand side, on the other hand, is only a function of the modulus, m. Hence, for given design parameters, Equation (3.39) can be solved for m which takes a value between zero and one. For mono-stable hard oscillations, case (i), the modulus satisfies $0 < m < 1/2$, whereas for the bi-stable inter-well oscillations, case (iii) (b), $1/2 < m < 1$. Using the resulting modulus value, the steady-state amplitude of the dimensionless response can be obtained using the amplitude relation given by Equations (3.38).

Along similar lines, it is possible to write the equation for the modulus of the elliptic function for case (ii) as

$$A^2 = -\frac{\zeta_T S_2}{\omega^2 \zeta_3 S_4}, \tag{3.40}$$

Similarly, Equations (3.27) can be rewritten as

$$\begin{aligned} \omega^2 &= \frac{\bar{\mu}}{(1+m)}, \\ A^2 &= -\frac{2\bar{\mu}m}{\bar{\gamma}\,(1+m)}. \end{aligned} \tag{3.41}$$

Combining Equations (3.40) and (3.41) yields the following response equation

$$-\frac{\bar{\gamma}\zeta_T}{2\bar{\mu}^2\zeta_3} = -\frac{m\Gamma_{\text{sn}}}{(1+m)^2} = f_{\text{sn}}(m). \tag{3.42}$$

where $0 < m < 1$, and for case (iii) (a) as

$$-\frac{\bar{\gamma}\zeta_T}{2\bar{\mu}^2\zeta_3} = \frac{\Gamma_{\text{dn}}}{(m-2)^2} = f_{\text{dn}}(m). \tag{3.43}$$

where, again, $0 < m < 1$.

It is worth mentioning that the linear response can be recovered by setting $\bar{\gamma} = 0$, which yields $m = 0$. In this scenario, the steady-state amplitude reduces to $A^2 = \frac{4}{3}\frac{\zeta_T}{\bar{\mu}\zeta_3}$ with $\text{cn}\,(\sqrt{\bar{\mu}}T_0 + \phi, 0) \equiv \cos\,(\sqrt{\bar{\mu}}T_0 + \phi)$ and $\text{sn}\,(\sqrt{\bar{\mu}}T_0 + \phi, 0) \equiv \sin\,(\sqrt{\bar{\mu}}T_0 + \phi)$.

3.5 Numerical Validations

To validate the asymptotic analytical solutions, the approximate analytical results are compared to a numerical integration of the equations of motion, Equation. (3.1a) and (3.1b). A harvester with square-sectioned bluff body with lift coefficients $a_1 = 2.5$ and $a_3 = 130$ is considered. The dimensionless response is obtained for three case studies depending on the values of $\bar{\mu}$ and $\bar{\gamma}$ as depicted in Fig. 3.2. Other parameters are kept constant as $\zeta_m = 3\times10^{-3}$, $\bar{m} = 6.83\times10^{-4}$, $\kappa = 1\times10^{-2}$ and $\alpha = 3$. Clearly, the difference between the results obtained analytically and numerically is negligible. This demonstrates the accuracy of the analytical approximations in predicting the response which provides a framework to conduct a comparative performance study between the different cases as discussed in the next chapter.

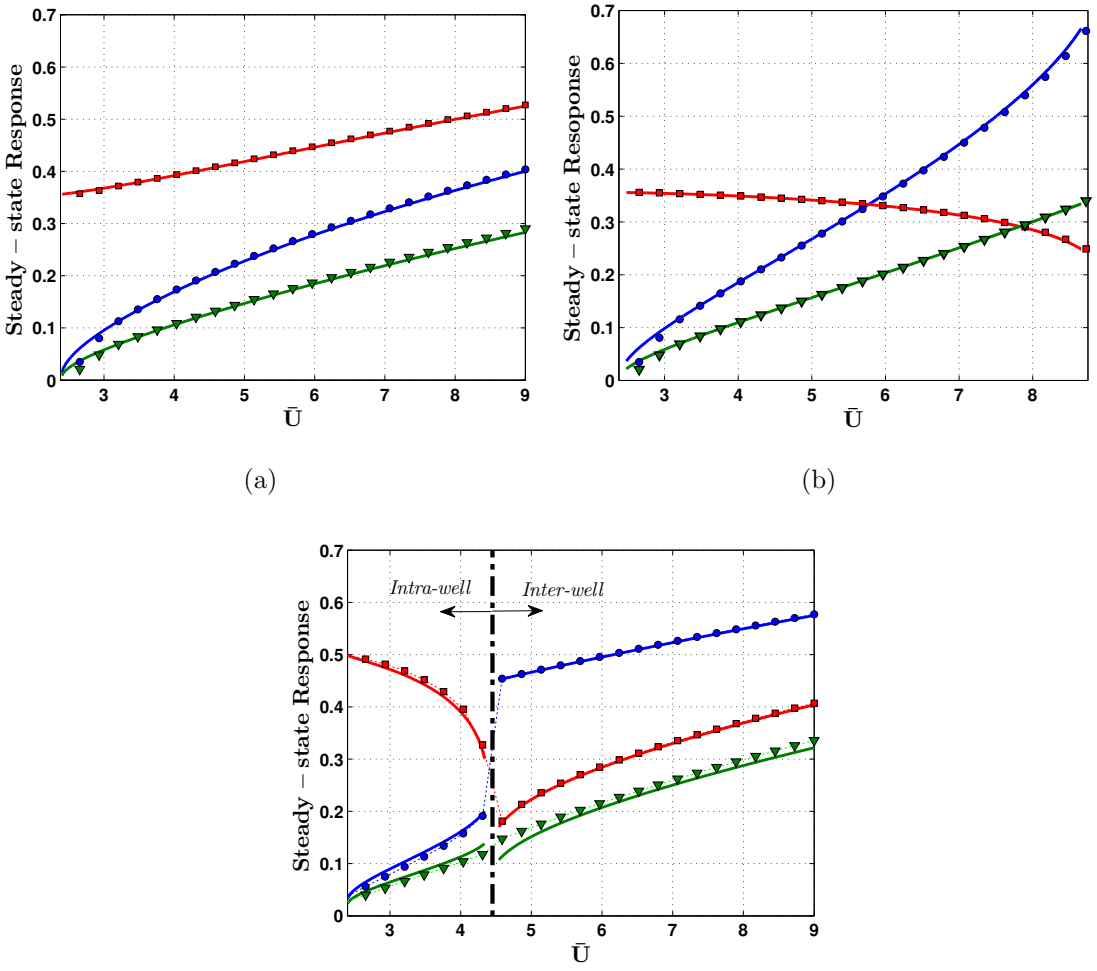

Figure 3.2: Variation of the dimensionless response with the dimensionless wind speed: (a) hardening with $\bar{\mu} = 5$ and $\bar{\gamma} = 50$ (b) softening with $\bar{\mu} = 5$ and $\bar{\gamma} = -7.5$ and (c) bi-stable with $\bar{\mu} = -5$ and $\bar{\gamma} = 50$. Solid lines represent analytical results while markers represent numerical results: (circle) for dimensionless amplitude $|\bar{y}|$, (triangle) for dimensionless voltage $|\bar{V}|$ and (square) for dimensionless frequency Ω.

Chapter 4

Optimization and Relative Performance Analysis

As discussed in Chapters 2 and 3, a nonlinear galloping FEH can outperform a linear one. Nevertheless, the harvested power is a function of many design parameters including the shape of the restoring force and the electric load resistance. This Chapter presents an investigation into the optimality of these two critical design parameters.

4.1 Power Optimization

In this section, we utilize the approximate analytical solution attained in Chapter 3 to obtain expressions for the harvested power and investigate the relative performance of galloping FEH exploiting different types of restoring force in their design. For a fair comparison, results are obtained at the optimal electric load which maximizes the output power.

The associated dimensional output power $|P|$ can be expressed as

$$|P| = |\bar{V}|^2 \frac{(\theta D)^2}{C_p} \alpha \omega_n, \tag{4.1}$$

and the optimal mechanical to electrical time-constant ratio α_{opt} embedded with the optimal load R_{opt} can be written as

$$\alpha_{opt} = \frac{1}{R_{opt} C_p \omega_n}, \tag{4.2}$$

Hence, the optimal power across this load can be calculated for each case different types of restoring force can expressed as:

- **Case (i): Hardening.**

  In this scenario, the dimensionless voltage expression obtained in Equation. (3.22) is utilized to find the steady-state amplitude of the dimensionless voltage $|\bar{V}|$ associated with the mono-stable hardening case as:

  $$|\bar{V}| = \frac{\pi m}{4\left(K_J - E_J\right)} \frac{\omega A}{\sqrt{\Omega^2 + \alpha^2}}, \tag{4.3}$$

  where the steady-state amplitude, A, and the frequency, ω, can be expressed as

  $$\begin{aligned} A &= \sqrt{\frac{2\bar{\mu} m}{\bar{\gamma}\left(1 - 2m\right)}}, \\ \omega &= \sqrt{\frac{\bar{\mu}}{\left(1 - 2m\right)}}. \end{aligned} \tag{4.4}$$

  Substituting Equation. (4.3) into Equation. (4.1) to attain a dimensional power expression for the hardening case. In order to optimize the harvested power with respect to the electric load, the first derivative of the power expression with respect to α is set to zero (i.e $\frac{d|P|}{d\alpha} = 0$), and by solving for α_{opt} we obtain

  $$\alpha_{opt} = \frac{\pi \sqrt{\bar{\mu}}}{2\sqrt{1 - 2m} K_J}, \tag{4.5}$$

The optimal electrical to mechanical time-constant expression is substituted then into the second derivative of the power with respect to α (i.e $\frac{d^2|P|}{d\alpha^2}$), which gives a negative value, therefore, at the value of α_{opt} the power is maximized. Hence, the optimal maximum power for the hardening case can be written as:

$$|P| = \frac{\pi}{8} \frac{m^3 K_J}{\sqrt{1-2m}^3 \left(E_J - K_J\right)^2} \frac{(\theta D)^2}{C_p} \frac{\omega_n}{\sqrt{|\bar{\mu}|}} \frac{\bar{\mu}^2}{|\bar{\gamma}|}. \tag{4.6}$$

- **Case (ii): Softening**

  The steady-state amplitude of the dimensionless voltage $|\bar{V}|$ associated with the mono-stable softening case can be written as

$$|\bar{V}| = \frac{\pi m}{4\left((1-m)K_J - E_J\right)} \frac{\omega A}{\sqrt{\Omega^2 + \alpha^2}}, \tag{4.7}$$

  where the steady-state amplitude, A, and the frequency, ω, are defined by

$$\begin{aligned} A &= \sqrt{-\frac{2\bar{\mu}m}{\bar{\gamma}\left(1+m\right)}}, \\ \omega &= \sqrt{\frac{\bar{\mu}}{(1+m)}}. \end{aligned} \tag{4.8}$$

  Similar to the hardening case, optimization analysis is conducted, and the optimal mechanical to electrical time-constant, α_{opt}, can be defined for the softening case by

$$\alpha_{opt} = \frac{\pi\sqrt{\bar{\mu}}}{2\sqrt{1+m}K_J}, \tag{4.9}$$

  while the associated maximum power can be written as

$$|P| = \frac{\pi}{8} \frac{m^3 K_J}{\sqrt{1+m}^3 \left(E_J - (1-m)K_J\right)^2} \frac{(\theta D)^2}{C_p} \frac{\omega_n}{\sqrt{|\bar{\mu}|}} \frac{\bar{\mu}^2}{|\bar{\gamma}|}. \tag{4.10}$$

- **Case (iii)a: Bi-stable intra-well oscillations.**

  For the bi-stable intra-well motion, which represents a softening asymmetric oscillations, the steady-state amplitude of the dimensionless voltage, $|\bar{V}|$, can be defined as

$$|\bar{V}| = \frac{1}{2}\frac{m\omega A}{\sqrt{(2\Omega)^2 + \alpha^2}}, \tag{4.11}$$

here, the steady-state amplitude, A, and the frequency, ω can be written as

$$\begin{aligned} A &= \sqrt{-\frac{2\bar{\mu}}{\bar{\gamma}\,(2-m)}}, \\ \omega &= \sqrt{\frac{-\bar{\mu}}{(2-m)}}. \end{aligned} \tag{4.12}$$

Along similar lines, the optimal mechanical to electrical time-constant α_{opt} for the bi-stable intra-well case can be defined as

$$\alpha_{opt} = \frac{\pi\sqrt{-\bar{\mu}}}{\sqrt{2-m}K_J}, \tag{4.13}$$

and the associated maximum power is calculated as

$$|P| = \frac{1}{4\pi}\frac{m^2 K_J}{\sqrt{2-m}^3}\frac{(\theta D)^2}{C_p}\frac{\omega_n}{\sqrt{|\bar{\mu}|}}\frac{\bar{\mu}^2}{|\bar{\gamma}|}. \tag{4.14}$$

- **Case (iii)b: Bi-stable inter-well oscillations.**

  In this case, the steady-state amplitude of the dimensionless voltage, $|\bar{V}|$, is similar to the hardening case as in Equation. 4.3 with the only difference in the expressions of the steady-state amplitude, A, and the frequency, ω as

$$\begin{aligned} A &= \sqrt{\frac{2\bar{\mu}m}{\bar{\gamma}\,(2m-1)}}, \\ \omega &= \sqrt{\frac{\bar{\mu}}{(2m-1)}}. \end{aligned} \tag{4.15}$$

  Hence, α_{opt} can be expressed as

$$\alpha_{opt} = \frac{\pi\sqrt{-\bar{\mu}}}{2\sqrt{2m-1}K_J},, \tag{4.16}$$

and the associated maximum power can be written as

$$|P| = \frac{\pi}{8} \frac{m^3 K_J}{\sqrt{2m-1}^3 \left(E_J - K_J\right)^2} \frac{(\theta D)^2}{C_p} \frac{\omega_n}{\sqrt{|\bar{\mu}|}} \frac{\bar{\mu}^2}{|\bar{\gamma}|}. \tag{4.17}$$

The optimal maximum power for case (i), case (ii), and case(iii) (a) and (b), respectively, can be defined as

$$\frac{|P|}{P_0^*} = \frac{\pi}{8} \frac{m^3 K_J}{\sqrt{1-2m}^3 \left(E_J - K_J\right)^2}, \tag{4.18a}$$

$$\frac{|P|}{P_0^*} = \frac{\pi}{8} \frac{m^3 K_J}{\sqrt{1+m}^3 \left(E_J - (1-m)K_J\right)^2}, \tag{4.18b}$$

$$\frac{|P|}{P_0^*} = \frac{1}{4\pi} \frac{m^2 K_J}{\sqrt{2-m}^3}, \tag{4.18c}$$

$$\frac{|P|}{P_0^*} = \frac{\pi}{8} \frac{m^3 K_J}{\sqrt{2m-1}^3 \left(E_J - K_J\right)^2}, \tag{4.18d}$$

where $P_0^* = \frac{(\theta D)^2}{C_p} \frac{\omega_n}{\sqrt{|\bar{\mu}|}} \frac{\bar{\mu}^2}{|\bar{\gamma}|}$.

4.2 Universal Curves

When inspecting Equation (4.18), it can be clearly seen that, for all cases considered, the dimensionless harvested power depends only on the modulus, m, which, in turn, is only a function of the parameter $-\frac{|\bar{\gamma}|}{2\bar{\mu}^2}\zeta_T$, as can be seen from the expressions for $f_{\mathrm{cn}}(m)$, $f_{\mathrm{sn}}(m)$ and $f_{\mathrm{dn}}(m)$ in Equations (3.39), (3.42), and (3.43), respectively. At the optimal load, ζ_e within ζ_T can be further approximated by

$$\zeta_e \approx \frac{\kappa}{2\sqrt{|\bar{\mu}|}}, \tag{4.19}$$

leading to

$$\zeta^* \approx \frac{\zeta_1 + \kappa/(2\sqrt{|\bar{\mu}|})}{\zeta_3}. \tag{4.20}$$

Hence, one can correctly surmise that there exists a unique parametric curve in the $\frac{|P|}{P_0^*} \times -\frac{|\bar{\gamma}|}{2\bar{\mu}^2}\zeta^*$ space that accurately represents each of the previous cases considered regardless of the other design parameters. These curves permit drawing critical conclusions regarding the relative performance for different types of nonlinearities as long as the bluff body is the same.

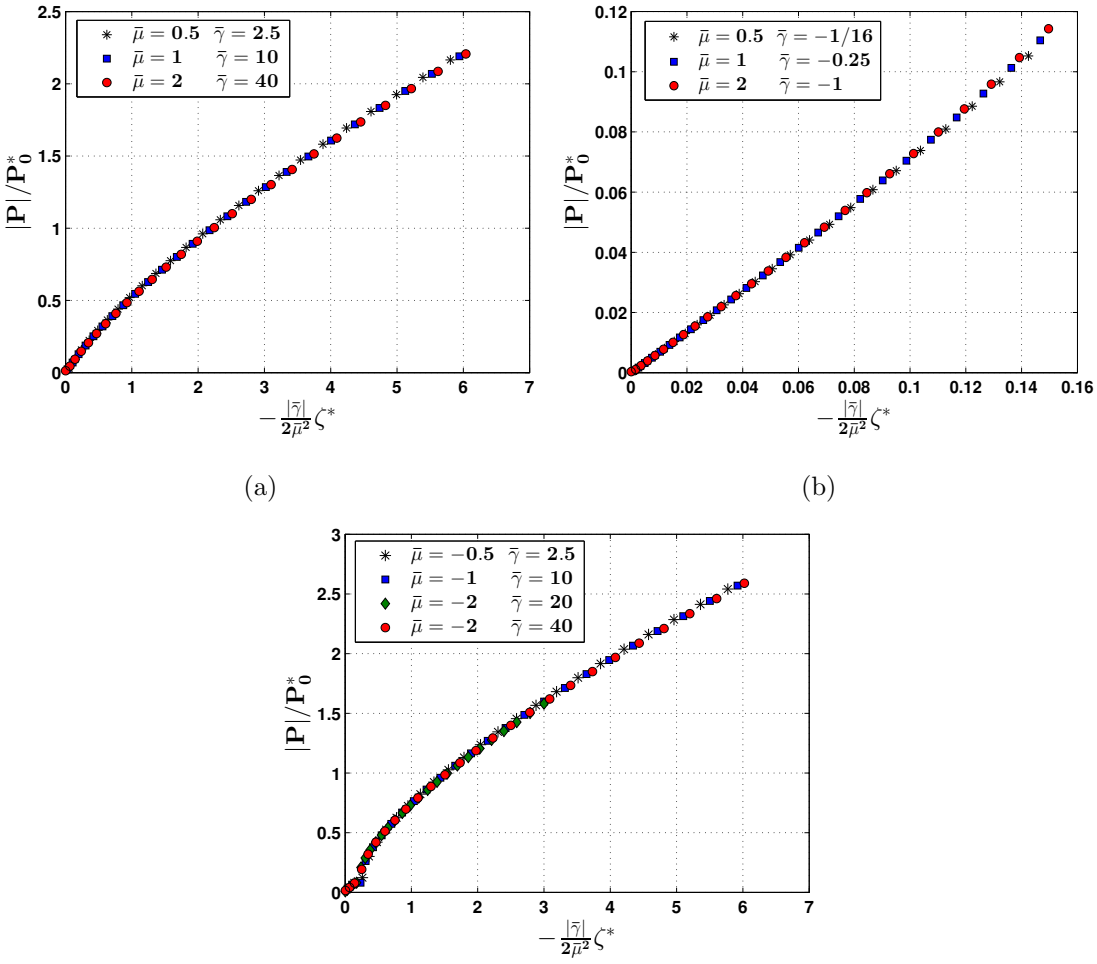

Figure 4.1: Universal power curves for the (a) hardening, (b) softening, and (c) bi-stable.

Figure 4.1 depicts these universal design curves for hardening, softening, and bi-stable flow energy harvesters incorporating different values of $\bar{\mu}$ and $\bar{\gamma}$ but similar flow and other design parameters. As clearly evident, no matter how $\bar{\mu}$ and $\bar{\gamma}$

are changed, the curves collapse nicely into a single universal design curve in the $\frac{|P|}{P_0^*} \times -\frac{|\bar{\gamma}|}{2\bar{\mu}^2}\zeta^*$. The reader should also bear in mind that a strongly nonlinear restoring force not only alters the amplitude and frequency of the signal but can also distort its shape from the perfect sinusoid. As such, for an accurate representation of the results, the average harvested power is considered as a performance measure. To that end, the trigonometric output voltage in Equations (3.22), (3.29), and (3.29) is approximated in terms of Jacobi elliptic functions and the average Root Mean Square (RMS) power is calculated over one period $4K_J$.

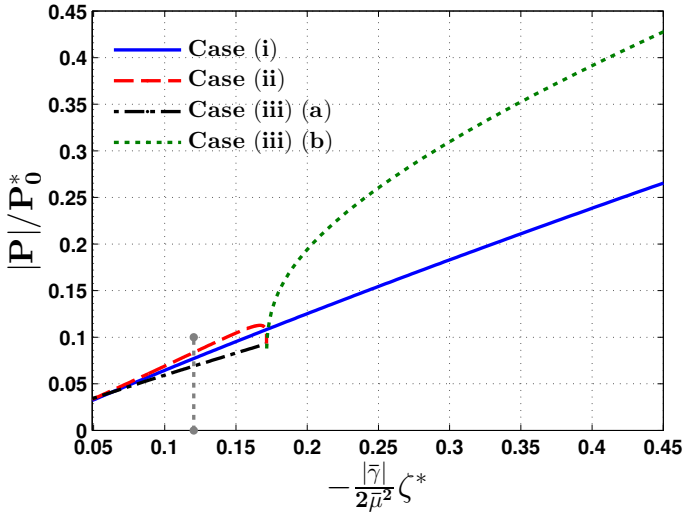

Figure 4.2: Variation of the dimensionless average harvested power with the design factor.

Variation of the resulting average power with the design factor is depicted in Fig. 4.2 for all types of restoring forces considered. The curves have been generated for a square-sectioned bluff body but can also be generated for any shape with different values of a_1 and a_3. This set of curves can serve as a complete design guide for choosing the shape of the potential function to enhance performance. For instance, based on Fig. 4.2, and for similar design parameters, i.e. similar coupling, mechanical damping, bluff body, and values (magnitude) of $\bar{\mu}$ and $\bar{\gamma}$, a FEH incorporating a softening restoring force outperforms the hardening design at the optimal load-

ing conditions up to the point where the dynamic trajectories associated with the softening system escape from the potential barrier resulting in a loss of stability. Similarly, it can be clearly seen that, the FEH with a mono-stable hardening restoring force outperforms the bi-stable harvester as long as oscillations are confined to a single potential well, i.e., intra-well oscillations. These results are further verified numerically by studying variation of the harvested RMS power with the electric load, represented by α, for the three cases considered and similar values of $\bar{\mu}$ and $\bar{\gamma}$ as depicted in Fig. 4.3. By comparing the peaks of the power curves presented in Fig.4.3 with circles, it is clear that the harvester with the softening design outperforms the one with hardening design which, in turn, outperforms the one performing intra-well oscillations.

Figure 4.2 also demonstrates that, in the region where the inter-well oscillations of the bi-stable harvester are excited, i.e. $-\frac{|\bar{\gamma}|}{2\bar{\mu}^2}\zeta^* \geq 0.17$, the bi-stable harvester clearly outperforms the mono-stable hardening design for the same values of $\bar{\mu}$ and $\bar{\gamma}$. For arbitrary values of $\bar{\mu}$ and $\bar{\gamma}$, one can simply calculate the value of $-\frac{|\bar{\gamma}|}{2\bar{\mu}^2}\zeta^*$ for the three different cases, then use the curves to find and compare the associated average power $|P|$.

4.3 Numerical Case Study

Inspecting Fig. 4.2 also reveals that, when two harvesters possessing the same type of restoring force, i.e. softening or hardening or bi-stable, have the same value of the design ratio $\frac{|\bar{\gamma}|}{\bar{\mu}^2}$, then the harvester with the smaller value of $\bar{\mu}$ provides higher output power levels at the same wind speed. This stems from the fact that, while the two harvesters have the same value of dimensionless power $|P|/P_0^*$, the dimensional power is inversely proportional to $\sqrt{\mu}$ given that ω_n, C_p, θ, and D are kept constant. This is further illustrated numerically by studying variation of the

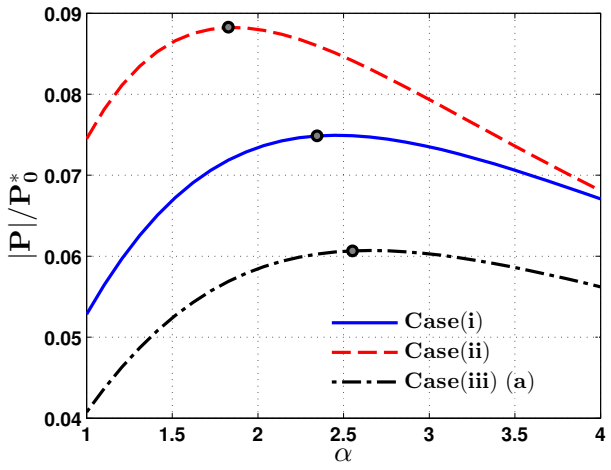

Figure 4.3: Variation of the RMS power $|P|$ with α for Case (i), (ii), and (iii). Results are obtained numerically for $|\bar{\mu}| = 5$, $|\bar{\gamma}| = 7.5$, $\bar{U} = 7.5$, $-\frac{|\bar{\gamma}|}{2\bar{\mu}^2}\zeta^* = 0.12$. Circles represent peak power.

harvested optimal power for different values of $\bar{\mu}$ and $\bar{\gamma}$ for case (i), case (ii), and case (iii), as shown, respectively, in Fig. 4.4. For instance, by comparing the power curves in Fig. 4.4 (a), one can clearly see that the harvester with ($\bar{\mu} = 0.5$,$\bar{\gamma} = 2.5$) outperforms the harvester with ($\bar{\mu} = 1$, $\bar{\gamma} = 10$) while the later, in turn, outperforms the one with ($\bar{\mu} = 2$,$\bar{\gamma} = 40$) even when the three harvesters have the same ratio of $\frac{|\bar{\gamma}|}{\bar{\mu}^2} = 10$. Notice that the same conclusion can be made by comparing the power curves corresponding to ($\bar{\mu} = 0.5$,$\bar{\gamma} = -1/16$), ($\bar{\mu} = 1$,$\bar{\gamma} = -0.25$), and ($\bar{\mu} = 2$,$\bar{\gamma} = -1$) in Fig. 4.4 (b) for case (ii) or ($\bar{\mu} = -0.5$,$\bar{\gamma} = 2.5$), ($\bar{\mu} = -1$,$\bar{\gamma} = 10$), and ($\bar{\mu} = -2$,$\bar{\gamma} = 40$) in Fig. 4.4 (c) for case (iii).

When comparing the output power curves in Fig. 4.4, it can be further concluded that, if two harvesters possessing the same type of restoring force have the same value of $\bar{\mu}$ but different values of $\bar{\gamma}$, then the harvester with the smaller $\bar{\gamma}$, including the negative values, will provide more output power. For example, the linear harvester with ($\bar{\mu} = 1$,$\bar{\gamma} = 0$) outperforms the harvester with hardening nonlinearity ($\bar{\mu} = 1$,$\bar{\gamma} = 10$), while the softening harvester with ($\bar{\mu} = 1$,$\bar{\gamma} = -0.25$) outperforms the linear harvester.

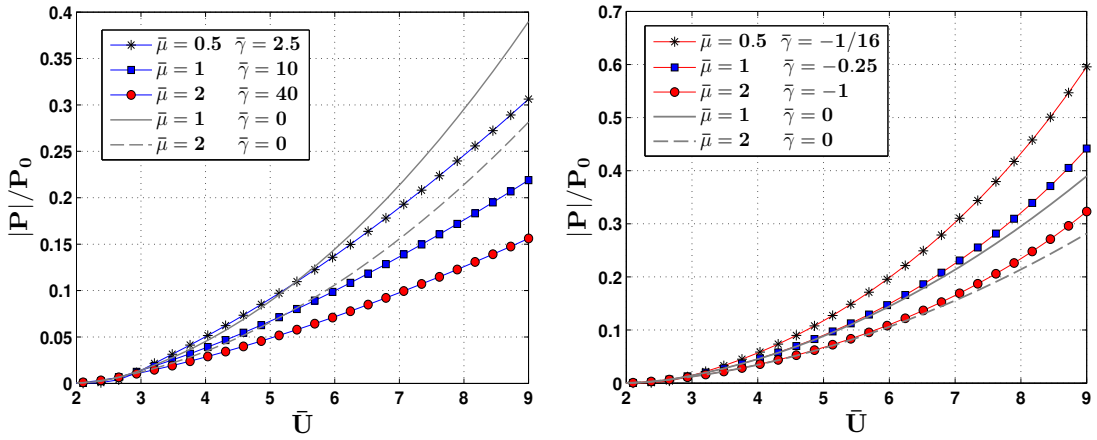

(a) (b)

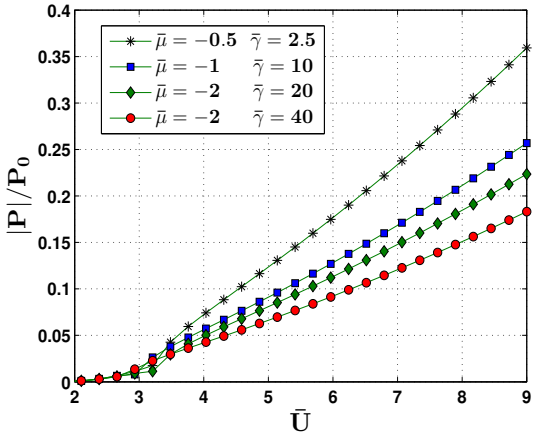

(c)

Figure 4.4: Variation of the optimal power with the dimensionless wind speed for different configurations of (a) case (i), (b) case (ii), and (c) case (iii). Here, $P_0 = \frac{(\theta D)^2 \omega_n}{C_p}$.

Chapter 5

Response of Wake-Galloping Flow Energy Harvesters to Single-Frequency Periodic Excitations

5.1 Motivations

Wake-galloping represents one of the most common types of fluid-structural coupling mechanisms used for flow energy harvesting. Typically, as shown in Fig. 5.1 (a), a wake-galloping FEH consists of a mechanical oscillator coupled to an energy harvesting circuit through an electromechanical transduction element which can either be piezoelectric, electromagnetic, electrostatic, or magnetostrictive. The oscillator is placed in the downstream of a bluff body or an obstacle. When an initially uniform fluid flows over the obstacle, it may undergo symmetry breaking in the form of a Von Kármán vortex street shedding from the trailing edge of the obstacle. The range

of flow velocities for which a periodic Von Kármán vortex street can be initiated depends on the *Reynolds* number of the flow. For circular cylinders and very small *Reynolds* numbers, $Re \lesssim 40$, the shear layer does not have enough energy to detach from the trailing edge and the vortices remain confined to a recirculation bubble adjacent to the obstacle walls. However, as the *Reynolds* number is increased beyond $Re \approx 40$, the shear layer detaches and periodic vortex shedding occurs as a result of a Hopf bifurcation. A fast Fourier transform of the time series of the resulting flow velocity reveals a dominant frequency up to approximately $Re \approx 10^5$ [45]. Beyond this value of the *Reynolds* number quasi-periodic and chaotic flow patterns can be observed.

For the wide range of Re numbers where the vortex shedding is periodic, the shed vortices induce a periodic lift on the mechanical oscillator placed in the downstream of the bluff body. In the *lock-in* region where the vortex shedding frequency is close to the natural frequency of the oscillator, the flow couples to the natural mode of the harvester resulting in large-amplitude motions. This results in kinetic energy transfer from the flow to the oscillator, which can be transformed into electricity using the electromechanical transduction element.

Wake galloping has several advantages over the traditional rotary-type generators which are known to suffer serious scalability issues because their efficiency drops significantly as their size decreases [59]. This is a result of relatively high viscous drag on the blades at low *Reynolds* numbers [60], electromagnetic interferences, and mechanical/thermal losses which increase as size decreases. Wake-galloping FEHs, on the other hand, operate using a very simple motion mechanism made from very few parts that would require little maintenance. They can be scaled to fit the desired application; and, most importantly, they can be designed to harvest energy from unsteady flow conditions which targets a niche market that traditional rotary-type generators do not address.

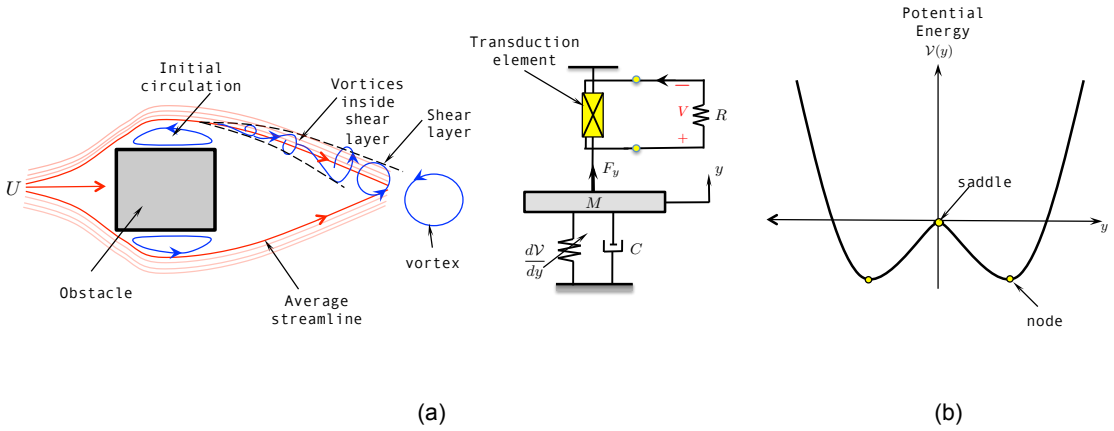

Figure 5.1: (a) A schematic of a nonlinear wake-galloping energy harvester. (b) The associated potential energy function. In the figure, R represents the electric load, $\mathcal{V}(y)$ represents the potential energy function of the oscillator, C is a viscous damping coefficient, F_y is the lift force, and V is the output voltage.

Nevertheless, wake-galloping FEHs have their own shortcomings. Typically, a wake-galloping FEH has a linear restoring force [30, 46], which results in a very narrow *lock-in* region. As a result, they do not respond well to the broad range of shedding frequencies normally associated with a variable flow speed. To enhance their response bandwidth under varying flow speeds, we propose exploiting stiffness nonlinearities in the form of a bi-stable restoring force. As shown in Fig. 5.1 (b), a bi-stable potential energy function consists of two potential wells (stable nodes) separated by a potential barrier (unstable saddle). Consequently, when the harvester interacts with the vortical structures generated by the obstacle, it can either perform small-amplitude resonant motions within a single potential well (intra-well motion); or large-amplitude non-resonant motions between the two potential wells (inter-well motion). It is widely accepted that the inter-well dynamics allow a harmonic oscillator to couple to the excitation over a wider range of frequencies.

This same concept has been used to improve the efficacy of vibratory energy harvesters (VEHs) [44, 48, 49]. Previous research findings indicated that, a carefully-

designed nonlinear vibratory energy harvester has a wider steady-state bandwidth as compared to an equivalent linear device [50, 51, 52, 19]. Furthermore, a comparative uncertainty propagation analysis performed on linear and nonlinear VEHs indicated that the linear device is much more sensitive to uncertainties arising from imprecise characterization of the host environment and/or from manufacturing tolerances [53]. Such promising findings formed the basis of the work presented in this Chapter.

The main objective of this work is to show that, by exploiting a bi-stable restoring force, the steady-state bandwidth of wake-galloping FEHs can be broadened, and, thereby their sensitivity to variations in the flow speed can be decreased. To achieve this goal, an experimental case study is carried out in a wind tunnel to compare the performance of bi-stable and linear FEHs under single- and multi-frequency vortex streets. A lumped-parameters model of the bi-stable harvester is introduced and solved using the method of multiple scales. The analytical solution is validated against experimental data and used to study the influence of the shape of the potential energy function on the output voltage of the harvester.

5.2 Experimental Investigation

This section investigates the response of the bi-stable wake-galloping FEH for the range of Re numbers where the vortex shedding has a single dominant frequency. To this end, we construct the piezoelectric wake-galloping FEH shown in Fig. 5.2. The mechanical oscillator consists of a $95 \times 12.5 \times 0.2$ mm^3 stainless steel cantilever beam attached to a $25 \times 25 \times 50$ mm ^{3} square-sectioned bluff body at the free end. The transduction element is a piezoelectric microfiber composite (MFC) patch laminated onto the Stainless Steel beam. The obstacle which generates the Von Kármán vortex street is a square-sectioned cylinder of characteristics width, $D =$

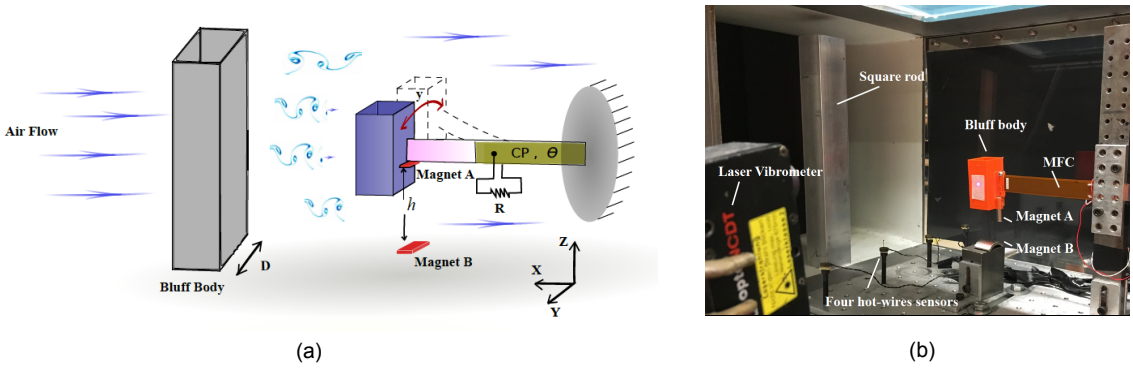

Figure 5.2: (a) A schematic of a cantilever beam-type wake-galloping FEH. (b) The associated experimental system.

42.5 mm.

The bi-stable restoring force is created by using two repulsive magnets, A, and, B, placed at a distance h as depicted in Fig. 5.2 (a). The shape of the potential energy function is altered by changing the distance between the two magnets [61]. For a small distance, $h \leq 25$ mm, the repulsive force between the magnets is large enough to cause the beam to buckle in the Y-direction, which, in turn, produces the bi-stable restoring force as shown in Fig. 5.3. In the absence of the lower magnet and for sufficiently small beam deformations, the potential function is quadratic and the restoring force can be approximated by a linear function of the tip deflection.

The harvester is placed in a wind tunnel as shown in Fig. 5.2 (b). The response of the bi-stable and linear harvesters is then compared as the wind speed is increased quasi-statically from 0.1 m/s to 10 m/s, ($270 \leq Re \leq 2.7 \times 10^4$). Both of the steady-state beam tip deflection and root-mean-square (RMS) voltage across a resistive load, $R = 100$ kΩ, are recorded.

Upon inspecting variation of the tip deflection with the wind speed as shown in Fig. 5.4 (a), it can be noted that the linear harvester exhibits the typical linear *lock-in* phenomenon where large-amplitude responses occur when the vortex shedding

frequency is close to the natural frequency of the linear harvester. This occurs in a small region approximately between $3 - 5.5$ m/s. As shown in Fig. 5.4 (b), the lock-in phenomenon remains unchanged for the backward sweep illustrating the non-hysteretic nature of the linear harvester.

The bi-stable harvester exhibits small-amplitude oscillations up to approximately 1.8 m/s. Below this speed, the dynamic trajectories remain confined to a single potential well. Near 1.8 m/s, the harvester starts performing large-amplitude periodic inter-well oscillations. These desirable oscillations persist up to approximately 6.3 m/s, where a jump to the small-amplitude branch of intra-well oscillations occurs. In the region where the bi-stable harvester performs inter-well oscillations, it clearly outperforms the linear harvester.

In the backward sweep shown in Fig. 5.4 (b), the harvester exhibits similar behavior with the main difference that the jump from small to large-amplitude motion occurs at lower speeds near 5.6 m/s, illustrating the hysteretic behavior of the nonlinear bi-stable harvester.

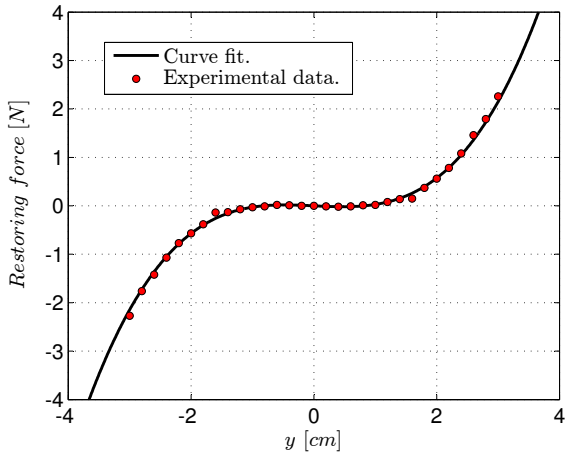

Figure 5.3: The restoring force of the harvester as obtained for h=22 mm. Markers represent experimental data and the solid line is a least-square cubic polynomial fit.

When inspecting the associated voltage response depicted in Figs. 5.5 (a) and (b), the enhanced bandwidth associated with the bi-stable harvester can still be observed in both directions of the frequency sweep. However, near the lower end of frequencies, the large-amplitude responses are not as prominent as the tip deflection. This can be attributed to the fact that the output voltage is directly proportional to the product of the tip deflection and associated frequency. As a result, the output voltage is reduced at the lower end of wind speeds.

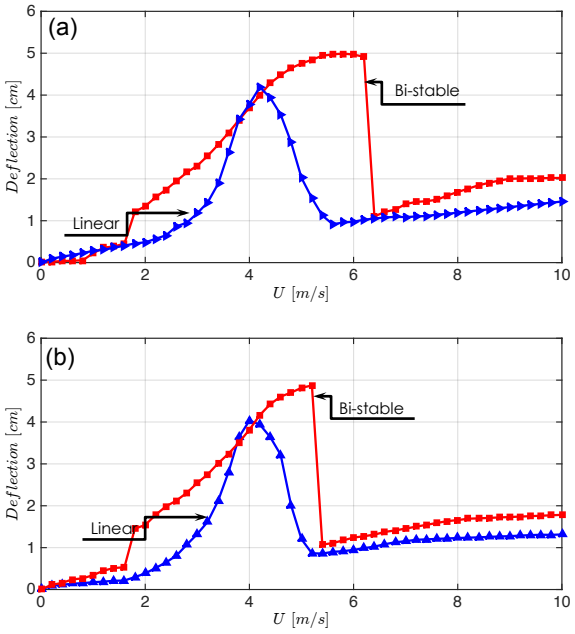

Figure 5.4: Variation of the harvester's tip deflection with the wind speed: (a) forward sweep, and (b) backward sweep.

5.3 Lumped-parameters Modeling

To better understand the response of the bi-stable harvester, we develop a lumped-parameters mathematical model of the system following Fig. 5.1 (a). In the proposed model, we assume that the dynamics of the piezoelectric beam can be captured by a single-degree-of-freedom (SDOF) harmonic oscillator with an effective mass, M,

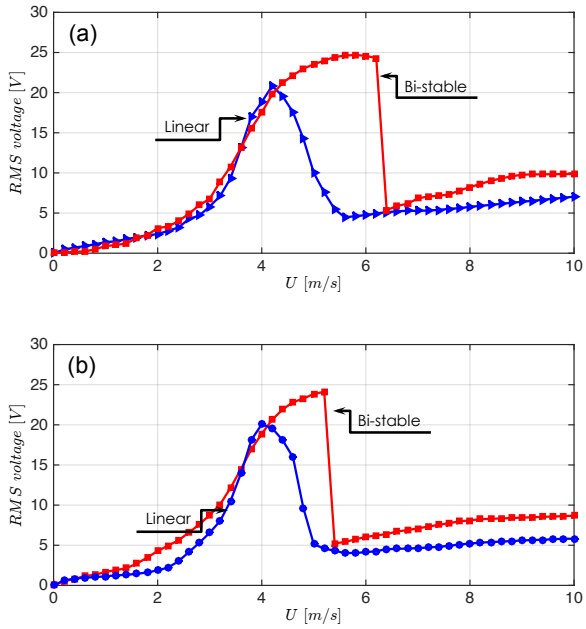

Figure 5.5: Variation of the harvester's RMS voltage with the wind speed: (a) forward sweep, and (b) backward sweep.

a restoring force, $\frac{d\mathcal{V}}{dy}$, and an effective damping coefficient, C. The assumption that a SDOF oscillator can be used to represent the beam's tip deflection near its first modal frequency is valid as long as the vortex shedding frequency is close to the first modal frequency of the beam, and the first mode is not in internal resonance with any of the other vibration modes.

When the beam, represented by the harmonic oscillator, is placed in the wake of the bluff body, it interacts with the Von Kármán vortex street. As a result, it undergoes harmonic oscillations in the cross-flow direction. This strains a piezoelectric element of capacitance, C_p, which, in turn, generates a voltage difference, V, across a resistive load, R. Upon implementing Newton's laws on the oscillator's mass and Kirchoff's voltage law across the closed-circuit loop, we obtain the equations governing the dynamics of the system as

$$M\ddot{y} + C\dot{y} + \frac{d\mathcal{V}}{dy} + \theta V = F_y, \tag{5.1a}$$

$$C_p\dot{V} + \frac{V}{R} - \theta\dot{y} = 0. \tag{5.1b}$$

Here, the dot represents a derivative with respect to time, t, θ is the electromechanical coupling coefficient, F_y, is the vertical lift force acting on the harvester's bluff body, and $\mathcal{V}$ is the potential energy function of the mechanical oscillator which, for a *Duffing* bi-stable potential, can be written in the general form: $\mathcal{V} = -\frac{1}{2}\mu y^2 + \frac{1}{4}\gamma y^4$. Here, $\mu > 0$ is a linear stiffness coefficient, and $\gamma > 0$ is a cubic stiffness coefficient. The values of μ and γ are empirically identified by measuring the restoring force depicted earlier in Fig. 5.3.

To model the vertical lift force, F_y, we use an uncoupled single-frequency force model as described in Ref. [62]. According to the single-frequency model, the lift force is given by:

$$F_y = \frac{1}{2}\rho U^2 D C_F \sin\left(2\pi S_t \frac{U}{D} t\right), \tag{5.2}$$

where ρ is the density of the flow per unit length, U is the speed of the mean flow, D is the cross-flow dimension of the obstacle, C_F is an empirical dimensionless lift force coefficient which depends on the geometry and aspect ratio of the bluff body, and S_t is the *Strouhal* number which, for the range of Re numbers considered, is almost constant at 0.13 [63].

5.4 Approximate Analytical Solution

To validate the nonlinear lumped-parameters model adopted in this Chapter, we obtain an approximate analytical solution of Equations (5.1a) and (5.1b) using the method of multiple scales. To this end, we first non-dimensionalize the equations by introducing the following dimensionless quantities:

$$\bar{t} = t\omega_n, \qquad \bar{y} = \frac{y}{D}, \qquad \bar{V} = \frac{C_p}{\theta D}V, \qquad \bar{m} = \frac{\rho D^2 C_F}{2M},$$
$$\bar{U} = \frac{U}{\omega_n D}, \qquad \kappa = \frac{\theta^2}{M\omega_n^2 C_p}, \qquad \alpha = \frac{1}{RC_p\omega_n}, \qquad \zeta_m = \frac{C}{2M\omega_n},$$

where ω_n is the natural frequency of the linear harvester at short-circuit, $\bar{y}$ and $\bar{V}$ represent the dimensionless transverse displacement and voltage respectively, $\bar{m}$ is the flow-to-harvester mass ratio, ζ_m is the mechanical damping ratio, $\bar{U}$ is the reduced wind speed, κ is the dimensionless electromechanical coupling, and α is the mechanical to electrical time-constant ratio.

The nondimensionalization yields the following dimensionless equations:

$$\bar{y}'' + 2\zeta_m \bar{y}' - \bar{\mu}\bar{y} + \bar{\gamma}\bar{y}^3 + \kappa\bar{V} = \bar{m}\bar{U}^2 \sin(\Omega\bar{t}), \tag{5.3a}$$

$$\bar{V}' + \alpha\bar{V} - \bar{y}' = 0, \tag{5.3b}$$

where the prime denotes a derivative with respect to the non-dimensional time $\bar{t}$, and

$$\bar{\mu} = \frac{\mu}{M{\omega_n}^2}, \qquad \bar{\gamma} = \frac{\gamma D^2}{M{\omega_n}^2}, \quad \Omega = 2\pi S_t \bar{U}.$$

5.4.1 Intra-well Response

First, we analyze the dynamics of the local intra-well oscillations, i.e., we obtain an approximate analytical solution of the response within a single potential well. To this end, we expand the system's dynamics about the local stable equilibria by introducing $\bar{y}_t = \bar{y} - y_e$, where $y_e = \pm\sqrt{\bar{\mu}/\bar{\gamma}}$ are the stable fixed points; this yields

$$\bar{y}_t'' + 2\zeta_m \bar{y}_t' + \omega_0^2 \bar{y}_t + \bar{\eta}\bar{y}_t^2 + \bar{\gamma}\bar{y}_t^3 + \kappa\bar{V}_t = \bar{m}\bar{U}^2 \sin(\Omega\bar{t}), \tag{5.4a}$$

$$\bar{V}' + \alpha\bar{V} - \bar{y}_t' = 0, \tag{5.4b}$$

where $\bar{y}_t$ represents the dynamic trajectories within a single potential well, $\omega_0 = \sqrt{2\bar{\mu}}$ is the local frequency of oscillation, and $\bar{\eta} = 3\sqrt{\bar{\mu}\bar{\gamma}}$ is a quadratic nonlinearity coefficient which reflects the asymmetric response within a single potential well.

To implement the method of multiple scales on Equations (5.4a) and (5.4b), we expand the time, and time derivatives into multiple time scales as:

$$T_0 = \bar{t}, \quad T_1 = \epsilon\bar{t}, \quad T_2 = \epsilon^2\bar{t}, \tag{5.5}$$

$$\begin{aligned}\frac{d}{d\bar{t}} &= D_0 + \epsilon D_1 + \epsilon^2 D_2 + \mathcal{O}(\epsilon^3),\\ \frac{d^2}{d\bar{t}^2} &= D_0^2 + \epsilon^2 D_1 + 2\epsilon D_0 D_1 + 2\epsilon^2 D_0 D_2 + \mathcal{O}(\epsilon^3),\end{aligned} \tag{5.6}$$

where ϵ is a scaling parameter, and $D_n = \frac{\partial}{\partial T_n}$. The dependent variables $\bar{y}_t$ and $\bar{V}$ are also expanded in the following form:

$$\begin{aligned}\bar{y}_t &= y_0(T_0, T_1, T_2) + \epsilon y_1(T_0, T_1, T_2) + \epsilon^2 y_2(T_0, T_1, T_2) + \mathcal{O}(\epsilon^3),\\ \bar{V} &= V_0(T_0, T_1, T_2) + \epsilon V_1(T_0, T_1, T_2) + \epsilon^2 V_2(T_0, T_1, T_2) + \mathcal{O}(\epsilon^3).\end{aligned} \tag{5.7}$$

For the harvester at hand, the damping ratio, flow-to-harvester mass ratio, quadratic and cubic nonlinearity coefficients, and electromechanical coupling are much smaller than $\mathcal{O}(1)$, and, hence can be scaled such that their effect appears at the second-order of the perturbation problem. To this end, we let

$$\zeta_m = \epsilon^2 \zeta_m, \quad \bar{m} = \epsilon^2 \bar{m}, \quad \bar{\eta} = \epsilon \bar{\eta}, \quad \bar{\gamma} = \epsilon^2 \bar{\gamma}, \quad \kappa = \epsilon^2 \kappa \tag{5.8}$$

Furthermore, since we are interested in the primary resonance behavior of the harvester within a single potential well, we express the nearness of the linearized oscillation frequency ω_0, to the excitation frequency, Ω, by introducing

$$\Omega = \omega_0 + \epsilon^2 \sigma \tag{5.9}$$

Here, σ, represents a small detuning parameter. Substituting Equations (5.5-5.9) into Equations (5.4a) and (5.4b), then collecting terms of equal powers of ϵ, we obtain:

$\mathcal{O}(\epsilon^0)$:

$$D_0^2 y_0 + \omega_0^2 y_0 = 0, \tag{5.10a}$$

$$D_0 V_0 + \alpha V_0 = D_0 y_0, \tag{5.10b}$$

$\mathcal{O}(\epsilon^1)$:

$$D_0^2 y_1 + \omega_0^2 y_1 = -2 D_0 D_1 y_0 - \bar{\eta} y_0^2, \tag{5.11a}$$

$$D_0 V_1 + \alpha V_1 = D_0 y_1 + D_1 y_0 - D_1 V_0, \tag{5.11b}$$

$\mathcal{O}(\epsilon^2)$:

$$D_0^2 y_2 + \omega_0^2 y_2 = \bar{m}\bar{U}^2 \sin(\Omega t) - D_1^2 y_0 - 2D_0 D_2 y_0 - 2D_0 D_1 y_1 - 2\zeta_m D_0 y_0 - 2\bar{\eta} y_0 y_1 - \bar{\gamma} y_0^3 - \kappa V_0, \tag{5.12a}$$

$$D_0 V_2 + \alpha V_2 = D_0 y_2 + D_2 y_0 + D_1 y_1 - D_2 V_0 - D_1 V_1. \tag{5.12b}$$

The zeroth-order perturbation problem presented by Equations (5.10a) and (5.10b) admits a solution of the form:

$$y_0 = A(T_1, T_2) e^{i\omega_0 T_0} + cc, \tag{5.13a}$$

$$V_0 = q_0 A(T_1, T_2) e^{i\omega_0 T_0} + cc, \tag{5.13b}$$

where $A(T_1, T_2)$ is a complex-valued function to be determined at a later stage in the analysis, $q_0 = (\omega_0^2 + i\alpha\omega_0)/(\omega_0^2 + \alpha^2)$, and cc is the complex conjugate of the preceding term. Here, we are solving for the steady state amplitude of the voltage perturbation equation, therefore, we eliminate the term $e^{-\alpha T_0}$. substituting Equations (5.13a) and (5.13b) into Equations (5.11a) and (5.11b), and eliminating terms that include $e^{\pm i\omega_0 T_0}$; i.e., the secular terms, we obtain

$$D_1 A(T_1, T_2) = 0. \tag{5.14}$$

This implies that A, is a function of the third time scale only, T_2. With this knowledge, the solution of the first-order problem represented by Equations (5.11a) and (5.10b) can be expressed as

$$y_1 = \frac{\eta}{\omega_0^2}\left(\frac{A^2}{3} e^{2i\omega_0 T_0} - A\bar{A}\right) + cc, \tag{5.15a}$$

$$V_1 = q_1 \frac{\eta A^2}{3} e^{2i\omega T_0} + cc, \tag{5.15b}$$

where $q_1 = (4\omega_0^2 + i2\alpha\omega_0)/(4\omega_0^2 + \alpha^2)$, and $\bar{A}$ is the complex conjugate of A. Upon substituting Equations (5.13a), (5.13a) and (5.15a) into Equation (5.12a), and eliminating secular terms, we obtain the following non-linear first-order differential equation to be solved for the unknown complex function, A:

$$-i\frac{\bar{m}\bar{U}^2}{2} e^{i\sigma T_0} - 2i\zeta_m \omega_0 A - \kappa q_1 A + \left(\frac{10\bar{\eta}^2}{3\omega_0^2} - 3\bar{\gamma}\right) A^2 \bar{A} = 0. \tag{5.16}$$

To solve Equation (5.16), we express the complex-valued function, A, in the polar form

$$A(T_2) = \frac{1}{2}a(T_2)e^{i\psi(T_2)}, \quad \bar{A}(T_2) = \frac{1}{2}a(T_2)e^{-i\psi(T_2)}, \tag{5.17}$$

where a and ψ represent, respectively, the unknown amplitude and phase of the response. Next, we substitute Equation (5.17) into Equation (5.16), then separate the real and imaginary parts of the outcome to obtain

$$D_2 a = -(\zeta_m + \zeta_e)a - \frac{\bar{m}\bar{U}^2}{2\omega_0}\cos\phi, \tag{5.18a}$$

$$aD_2\psi = (\sigma - \omega_s)a - \alpha_e a^3 + \frac{\bar{m}\bar{U}^2}{2\omega_0}\sin\phi, \tag{5.18b}$$

where $\phi = \sigma T_2 - \psi$, $\zeta_e = \frac{\alpha\kappa}{2(\omega_0^2+\alpha^2)}$ is a measure of the electric damping induced by the harvesting circuit, $\omega_s = \frac{\kappa\omega_0}{2(\omega_0^2+\alpha^2)}$ is a linear shift in the system's frequency due to the electric coupling, and $\alpha_e = \frac{1}{\omega_0}\left(\frac{3}{8}\bar{\gamma} - \frac{5\bar{\eta}^2}{12\omega_0^2}\right)$ represents the effective non-linearity coefficient.

In energy harvesting, one is generally more interested in analyzing the steady-state response of the system. To this end, we set the time derivatives in Equations (5.18a) and (5.18b) to zero, square and add the resulting equations to obtain the following nonlinear frequency-response equation:

$$\zeta_{eff}^2 a_0^2 + \left((\sigma - \omega_s)a_0 - \alpha_e a_0^3\right)^2 = \frac{\bar{m}^2\bar{U}^4}{4\omega_0^2}, \tag{5.19}$$

where $\zeta_{eff} = \zeta_m + \zeta_e$ is the effective damping, and a_0 is the steady-state amplitude.

The nonlinear frequency-response equation can be solved analytically for the steady-state amplitude, and depending on the forcing term and the excitation frequency, there exist one or three positive real-valued solutions. By assessing the eigenvalues of the associated Jacobian matrix, the stability of these solutions can be determined. The steady-state solutions for the intra-well oscillations can be expressed as

$$\bar{y}_t(\bar{t}) = a_0\cos(\Omega\bar{t} - \phi) + \frac{\bar{\eta}}{2\omega_0^2}\Big(-a_0^2 + \frac{1}{3}a_0^2\cos(2\Omega\bar{t} - 2\phi)\Big) + ..., \tag{5.20a}$$

$$\bar{V}(\bar{t}) = \frac{\omega_0}{\sqrt{\omega_0^2+\alpha^2}} a_0 \cos(\Omega\bar{t} - \phi + \psi_1) + \frac{\bar{\eta}}{3\omega_0\sqrt{4\omega_0^2+\alpha^2}} a_0^2 \cos(2\Omega\bar{t} - 2\phi + \psi_2) + ..., \tag{5.20b}$$

where

$$\phi = \tan^{-1}\left(\frac{\zeta_m}{(\sigma-\omega_s)-\alpha_e a_0^2}\right), \quad \psi_n = \tan^{-1}\left(\frac{\alpha}{n\omega_0}\right). \tag{5.21}$$

5.4.2 Inter-well Response

In this section, we study the global inter-well dynamic trajectories. Since the effective local stiffness around the unstable saddle is negative, it is not easy to implement the method of multiple scales in the traditional sense. To overcome this issue, we scale the damping, electromechanical coupling, and flow to harvester mass ratio at order ϵ, to get

$$\bar{y}'' - \bar{\mu}\bar{y} + \bar{\gamma}\bar{y}^3 = \mathcal{O}(\epsilon). \tag{5.22}$$

We assume that the solution of Equation (5.22) can be approximated by the first-order harmonic solution $\bar{y} = A\cos(\Omega\bar{t})$. Upon substituting the assumed solution into Equation (5.22), we obtain

$$-\Omega^2\bar{y} - \bar{\mu}\bar{y} + \bar{\gamma}\bar{y}^3 = \mathcal{O}(\epsilon). \tag{5.23}$$

Next, we add and subtract the term, $\Omega^2\bar{y}$, to the left-hand side of Equation (5.3a) and scale the damping, coupling, and mass ratio to be of order ϵ. This yields

$$\bar{y}'' + 2\epsilon\zeta_m\bar{y}' + \Omega^2\bar{y} + \epsilon(-\Omega^2\bar{y} - \bar{\mu}\bar{y} + \bar{\gamma}\bar{y}^3) + \epsilon\kappa\bar{V} = \epsilon\bar{m}\bar{U}^2\sin(\Omega\bar{t}), \tag{5.24a}$$

$$\bar{V}' + \alpha\bar{V} - \bar{y}' = 0, \tag{5.24b}$$

Substituting Equations (5.5) and (5.6) into Equation (5.24a) and (5.24b), truncating at the first order and collecting terms of equal powers of ϵ yields $\mathcal{O}(\epsilon^0)$:

$$D_0^2 y_0 + \Omega^2 y_0 = 0, \tag{5.25a}$$

$$D_0 V_0 + \alpha V_0 = D_0 y_0. \tag{5.25b}$$

$\mathcal{O}(\epsilon^1)$:

$$D_0^2 y_1 + \Omega^2 y_1 = \bar{m}\bar{U}^2 \sin(\Omega \bar{t}) - 2D_0 D_1 y_0 - 2\zeta_m D_0 y_0 - (-\Omega^2 y_0 - \bar{\mu} y_0 + \bar{\gamma} y_0^3) - \kappa V_0, \tag{5.26a}$$

$$D_0 V_1 + \alpha V_1 = D_0 y_1 + D_1 y_0 - D_1 V_0. \tag{5.26b}$$

The solution of the first-order equation can be written as

$$y_0 = A(T_1) e^{i\Omega T_0} + cc, \tag{5.27a}$$

$$V_0 = q_2 A(T_1) e^{i\Omega T_0} + cc, \tag{5.27b}$$

where $q_2 = (\Omega^2 + i\alpha\Omega)/(\Omega^2 + \alpha^2)$. Following the same steps used in the previous section, we obtain the following nonlinear equation for the unknown complex function, A:

$$2i\Omega D_1 A + 2i\zeta_m \Omega A - \left(\bar{\mu} + \Omega^2\right) A + 3\bar{\gamma} A^2 \bar{A} + \kappa q_2 A = \frac{\bar{m}\bar{U}^2}{2}. \tag{5.28}$$

Using the polar transformation of Equation (5.17), then separating the real and imaginary parts, we obtain the following equations for the amplitude and phase of the response:

$$D_1 a = -(\zeta_m + \zeta_e) a - \frac{\bar{m}\bar{U}^2}{2\Omega} \sin\phi, \tag{5.29a}$$

$$a D_1 \psi = -\frac{a}{2\Omega}\left(\Omega^2 + \bar{\mu} - \omega_s\right) + \frac{3\bar{\gamma}}{8\Omega} a^3 - \frac{\bar{m}\bar{U}^2}{2\Omega} \cos\phi, \tag{5.29b}$$

where $\zeta_e = \frac{\kappa\alpha}{2(\Omega^2+\alpha^2)}$, and $\omega_s = \frac{\kappa\Omega^2}{(\Omega^2+\alpha^2)}$. At steady state the previous equation yields the following nonlinear frequency-response equation governing the inter-well oscillations:

$$\zeta_{eff}^2 a_0^2 + \left(\Omega^2 + \bar{\mu} - \omega_s)\frac{a_0}{2\Omega} - \frac{3\bar{\gamma}}{8\Omega} a_0^3\right)^2 = \frac{\bar{m}^2 \bar{U}^4}{4\Omega^2}, \tag{5.30}$$

where $\zeta_{eff} = (\zeta_m + \zeta_e)$. Upon eliminating the secular terms in Equation (5.26a), and solving the resulting equation we obtain:

$$y_1 = \frac{\gamma a_0^3}{64\Omega^2} e^{3(i\Omega T_0 + \phi)} + cc, \tag{5.31}$$

and

$$V_1 = q_3 \frac{\gamma a^3}{64\Omega^2} e^{3(i\Omega T_0 + \phi)} + cc, \tag{5.32}$$

where $q_3 = \frac{9\Omega^2 + i3\alpha\Omega}{(9\Omega^2+\alpha^2)}$. Substituting Equations (5.31), (5.32), (5.27a) and (5.27b) into Equation (5.7), the approximate analytical solution of the inter-well dynamics can be expressed as

$$\bar{y}(\bar{t}) = a_0 \cos(\Omega\bar{t} + \phi) + \frac{\bar{\gamma} a_0^3}{32\Omega^2} \cos(3\Omega\bar{t} + 3\phi) + ..., \tag{5.33a}$$

$$\bar{V}(\bar{t}) = \frac{a_0\Omega}{\sqrt{\Omega^2+\alpha^2}} \cos(\Omega\bar{t}+\phi+\psi_1) + \frac{3\bar{\gamma} a_0^3}{32\Omega\sqrt{9\Omega^2+\alpha^2}} \cos(3\Omega\bar{t}+3\phi+\psi_3)+..., \tag{5.33b}$$

where

$$\phi = \tan^{-1}\left(\frac{8\zeta_{eff}\Omega}{4(\Omega^2+\bar{\mu}-\omega_s) - 3\bar{\gamma}a_0^2}\right) + \frac{3\bar{\gamma}}{8\Omega}a_0^3, \quad \psi_n = \tan^{-1}\left(\frac{\alpha}{n\Omega}\right). \tag{5.34}$$

5.5 Analytical Results and Experimental Validations

Using the approximate analytical solution obtained in the previous section, we study variation of the tip deflection and output voltage with the wind speed. Figure 5.6 reveals a more complex picture than initially predicted by the experimental results. Specifically, it can be observed that, for certain regions of the wind speed, multiple co-existing branches of solutions exist. Some of these solutions are stable (solid line) while other are unstable (dashed lines), and, are hence physically unrealizable. Figure 5.6 (b) provides a clearer picture of these coexisting branches of solutions for a small window of wind speeds extending up to $U = 2.5$ m/s. It can be clearly seen that there are three possible physically-realizable steady-state responses between $U \approx 0.4$ m/s and $U \approx 0.75$ m/s; these are the non-resonant branch of intra-well responses, S_n, the resonant branch of intra-well responses, S_r, and the large-orbit inter-well branch, S_L. Beyond $U \approx 0.75$ m/s, only the branches S_r and S_L coexist.

To explain how these coexisting solutions influence the performance of the harvester, we consider an experiment wherein the wind velocity is increased quasi-statically

from zero towards higher wind speeds. The harvester initially performs small-amplitude intra-well oscillations on the non-resonant branch of solutions, S_n, up to the point, cfA, which represents a cyclic-fold bifurcation in the deflection/voltage versus wind speed parameters space. As a result, the response jumps to one of the adjacent stable periodic solutions. Here, there are two possible adjacent solutions: the small-amplitude intra-well resonant solution, S_r, and the large-orbit inter-well solution, S_L. Due to the presence of two competing adjacent solutions, the final destination of the harvester is determined by the size of the competing basins of attraction of each one of these solutions and the initial conditions.

The basins of attraction of the competing solutions are shown in Fig. 5.7 (a) and

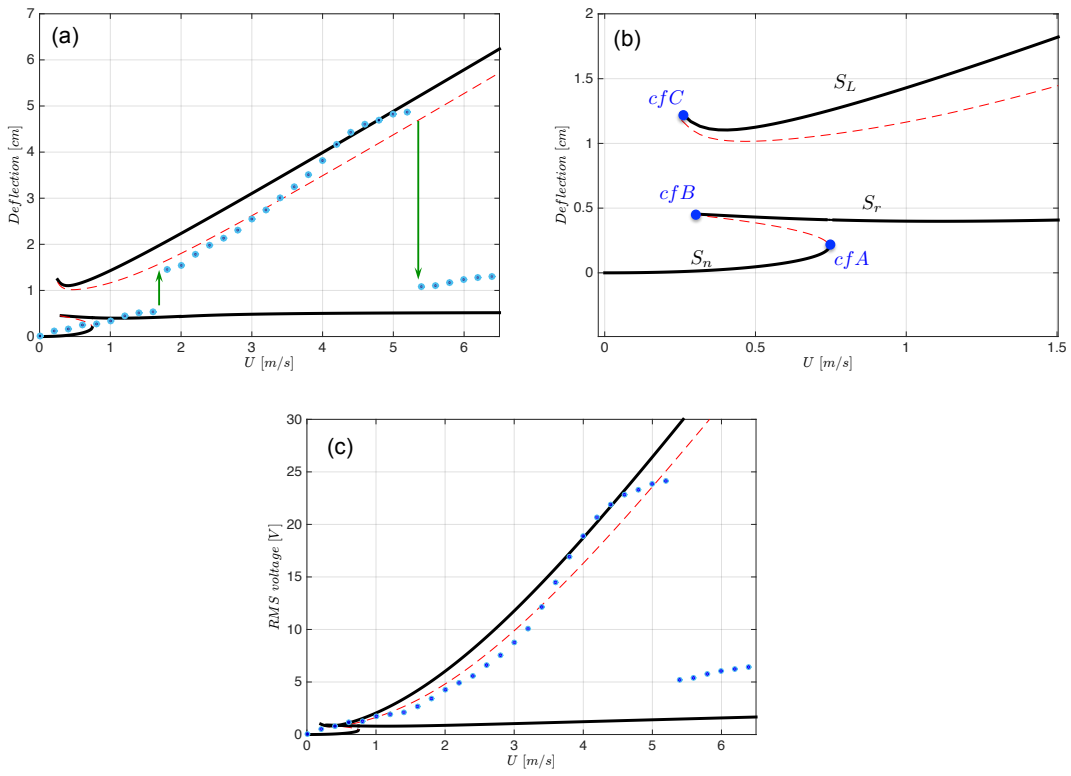

Figure 5.6: Variation of (a,b) the tip deflection and (c) the RMS voltage with the wind speed: solid lines represent stable periodic orbits, dashed lines represent unstable periodic orbits, and circles represent experimental results.

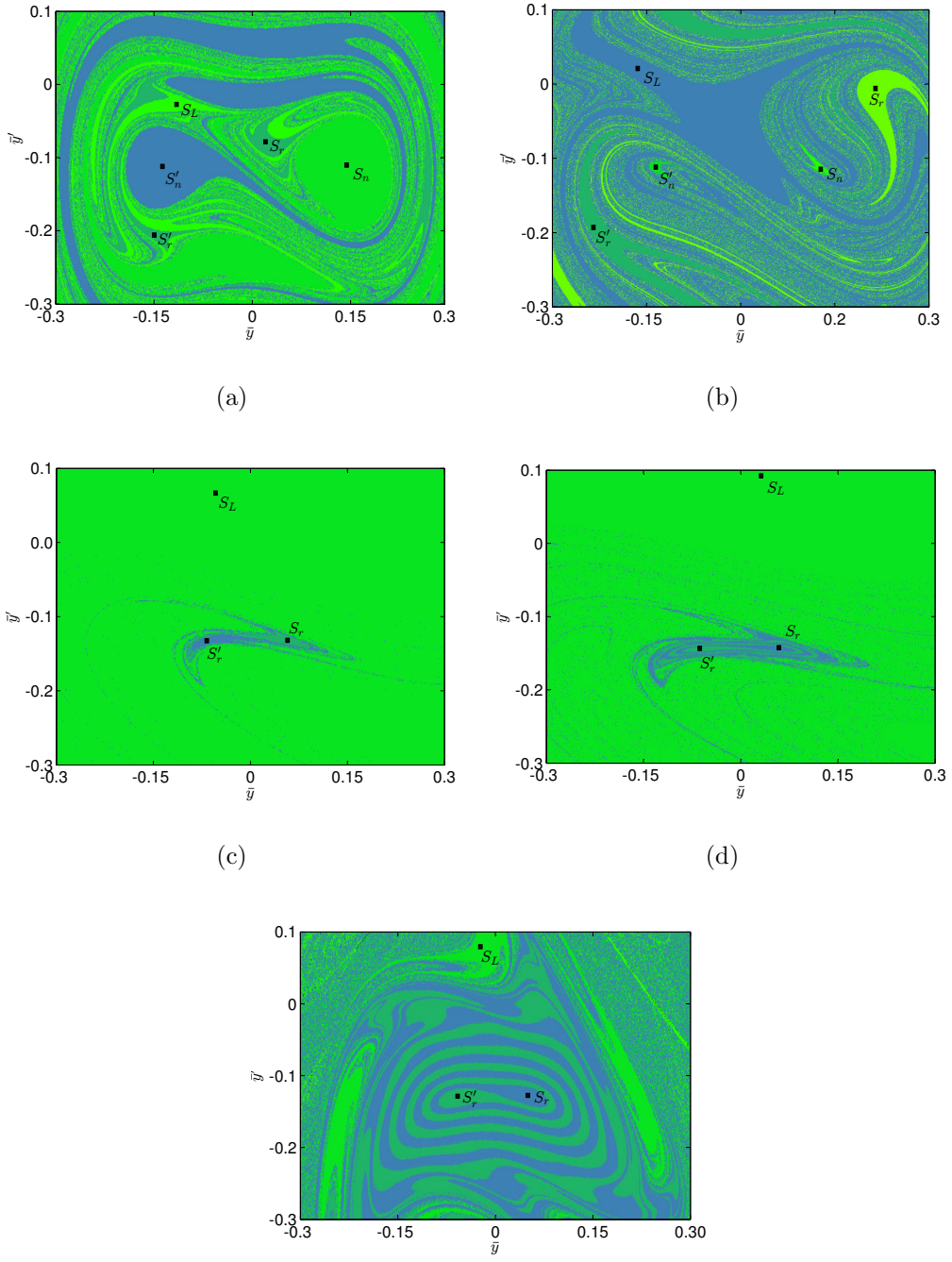

Figure 5.7: Basins of attraction of the harvester's response for (a) $U = 0.5$ m/s, (b) $U = 0.85$ m/s, (c) $U = 3$ m/s, (d) U=4 m/s, and (e) U=6 m/s

(b) for, respectively, $U = 0.5$ m/s, and $U = 0.85$ m/s. It is evident that the basin of attraction of the S_n branch is dominant when $U = 0.5$ m/s. As such, the harvester will most likely perform small amplitude intra-well oscillation when $U = 0.5$ m/sec. On the other hand, when the wind speed is increased to $U = 0.85$ m/sec, the basin of attraction associated with the S_n branch shrinks significantly while the basins of attraction of the S_r and S_L branches expand.

Results of the actual experiment, shown in Fig. 5.6 (a), corroborates the theoretical findings since the response jumps near $U = 0.85$ m/s to the branch S_r, and continues to follow this branch up to a speed of 1.8 m/s. At this point, the basin of attraction of the solution, S_r, becomes very small and the harvester's response jumps to the inter-well branch, S_L, whose basin of attraction becomes very large as illustrated in Figs. 5.7 (c) and (d). Further increase in the wind speed causes the amplitude of the harvester's response to increase following the branch S_L up to the point where its basin of attraction becomes very small. As a result, the harvester goes back to perform intra-well oscillations on the resonant branch, S_r. At this point, the basin of attraction of the resonant branch of intra-well solution, S_r, becomes dominant again as shown in Fig. 5.7 (e).

In theory, during a reverse wind sweep starting at the large-amplitude inter-well branch, S_L, the amplitude of the harvester's response decreases as the wind speed is decreased down to, cfC, where the response jumps down to the stable non-resonant branch of solutions, S_n, and the harvester starts to perform small-amplitude intra-well motions. However, the basin of attraction associated with S_L becomes too small before the wind speed decreases to the cyclic fold, cfC. As a result, the response jumps down to the lower branch of solution at much higher wind speeds.

The reason that, not all of the analytically predicted solutions can be resolved in the experiment, stems from two facts. Firstly, as shown in Fig. 5.7, some of the available stable solutions have very small basins of attraction, and hence, only a

careful selection of initial conditions permits finding these solutions experimentally. Secondly, the experimental results are limited by the resolution of the wind speed tuner in the wind tunnel, which has a minimum resolution of 0.1 m/s. As such, some of the complex dynamics near the lower-end of wind speeds cannot be replicated experimentally.

5.6 Influence of the Potential Function

In this section, we investigate the influence of the potential shape on the output voltage. Two performance metrics will be utilized to assess the influence of the potential function on the performance of the harvester. The first is the critical wind speed at which the cyclic-fold bifurcation, cfA occurs. The smaller the value of U corresponding to cfA, the lower the wind speed at which the harvester starts performing desirable large-amplitude motions. The second performance criterion is the magnitude of the RMS voltage resulting from the large-orbit inter-well motions.

First, we vary the depth of the potential wells while keeping the separation distance between the wells constant as shown in Fig. 5.8 (a). The associated voltage response shown in Fig. 5.8 (b) indicates that, for the range of potential depths considered, designing the potential function with shallower potential wells increases the magnitude of the inter-well voltage responses and decreases the value of the critical wind speed at which the response jumps from the small-orbit intra-well orbit to the desired large-orbit solution. As such, decreasing the depth of the potential wells seems to be favorable for the performance of bi-stable wake-galloping FEHs. However, it is worth noting that, the increase in response amplitude shown in Fig. 5.8 (b), is not only due to the reduced depth of the potential wells. In fact, if we continue to decrease the depth of the potential wells, the potential shape approaches a mono-

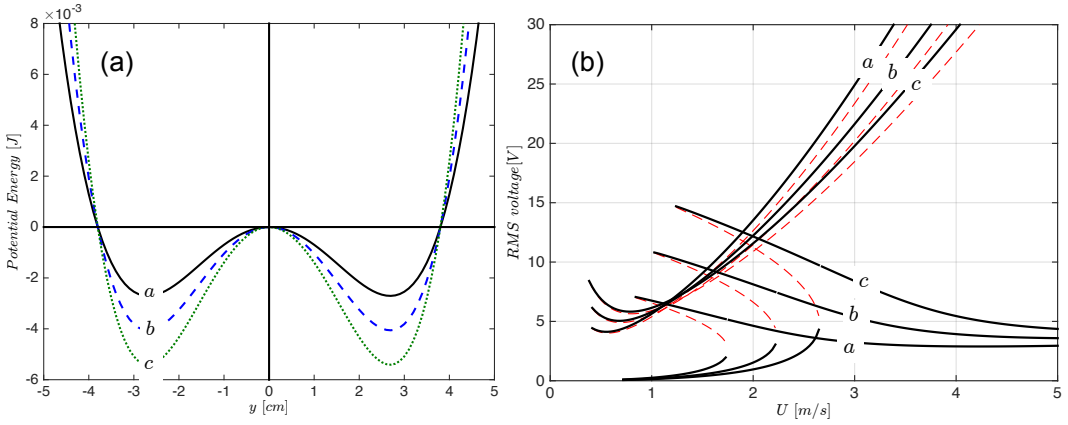

Figure 5.8: (a) Potential energy functions and (b) associated voltage response of the bi-stable harvester for different values of μ and γ. Results are obtained for the following three cases: case a: $\mu = 14.98$ N/m, $\gamma = 20734$ N/m^3, case b: $\mu = 22.47$ N/m, $\gamma = 31100$ N/m^3, and case c: $\mu = 29.96$ N/m, $\gamma = 41467$ N/m^3.

stable function in which case the large-orbit inter-well solution desirable for energy harvesting vanishes all together. A portion of the increased voltage is also due to the decrease in the slope of the potential function with respect to y, i.e., the restoring force, which becomes smaller for larger values of y. This yields a softer spring effect at larger deflection which tends to increase the output power.

We also study the influence of changing the distance between the potential wells while keeping the depth constant as shown in Fig. 5.9 (a). The resulting voltage curves shown in Fig. 5.9 (b) indicate that, as the distance between the potential wells increases, the amplitude of the large-orbit inter-well response increases, and the jump from the small-amplitude inter-well branch occurs at lower velocity. As such, for the range of parameters considered, increasing the separation distance between the potential wells while keeping the depth constant creates favorable conditions to improve the bandwidth of bi-stable wake-galloping FEHs. Finally, we investigate the more physically realistic case which involves varying the depth of the potential wells and the separation distance simultaneously. In this case, the voltage curves shown in 5.10 (b) reveal that, as the shape of the potential function is varied, the desirable

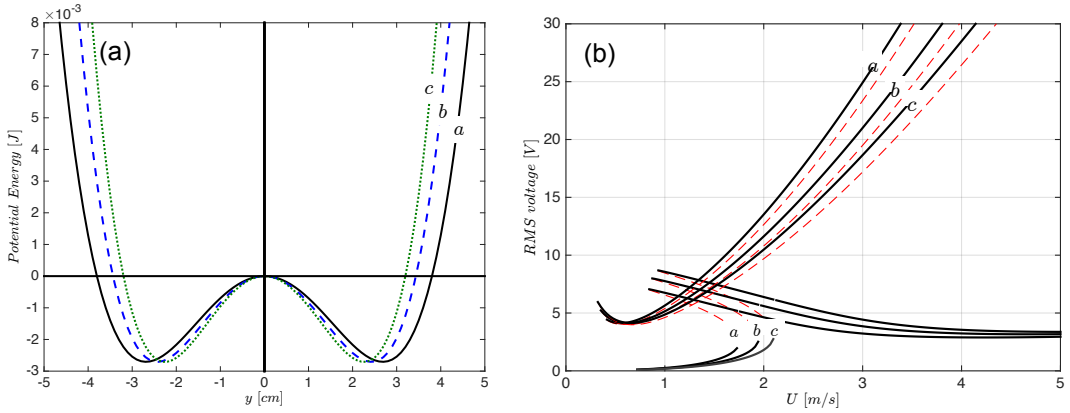

Figure 5.9: (a) Potential energy functions and (b) associated voltage response of the bi-stable harvester for different values of μ and γ. Results are obtained for the following three cases: case a: $\mu = 14.98$ N/m, $\gamma = 20734$ N/m^3, case b: $\mu = 18.35$ N/m, $\gamma = 31100$ N/m^3, and case c: $\mu = 21.20$ N/m, $\gamma = 41467$ N/m^3.

performance criteria; i.e., the minimum wind speed at which the jump to the large-orbit solution occurs, and the magnitude of the voltage in the inter-well region have a competing nature. For shallower potential wells and smaller separation distances

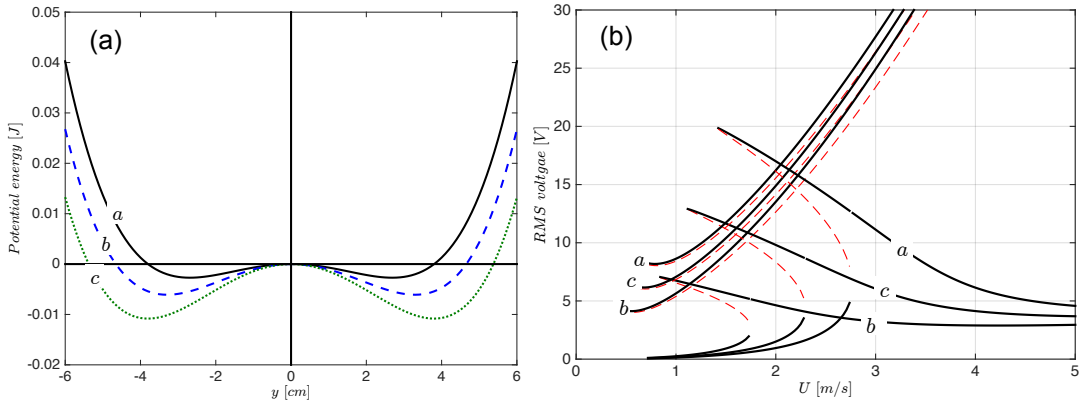

Figure 5.10: (a) Potential energy functions and (b) associated voltage response of the bi-stable harvester for different values of μ and γ. Results are obtained for the following three cases: case a: $\mu = 14.98$ N/m, $\gamma = 20734$ N/m^3, case b: $\mu = 22.47$ N/m, $\gamma = 20734$ N/m^3, and case c: $\mu = 29.96$ N/m, $\gamma = 20734$ N/m^3.

between the wells, the harvester starts performing large inter-well motions at lower wind speeds, but the resulting inter-well motions are generally smaller. On the other hand, for deeper potential wells and larger separation distances between the wells, the harvester starts performing large inter-well motions at higher wind speeds, but the resulting inter-well motions are generally larger. This demonstrates the presence of an optimal potential shape which can be used to maximize performance for given design parameters.

Chapter 6

Response of Wake-Galloping Flow Energy Harvesters to Multi-Frequency Excitations

The goal of this chapter is to experimentally investigate the performance of wake-galloping bi-stable FEHs under a multi-frequency vortex street and to comparing their performance to an equivalent linear device under similar flow conditions.

6.1 Experimental Setup

A similar setup to the one used previously and shown in Fig. 6.1 is used in the section. The only difference is that, as shown in Fig. 6.1, multi-frequency flow excitation is generated using grids located at the upstream of the bluff body [64]. This approach has been widely used in the open literature to generate unsteady wakes and controlled turbulence in a wind tunnel. The key parameters which control the Reynolds number, Re, and thereby the nature of the wake behind the grids are

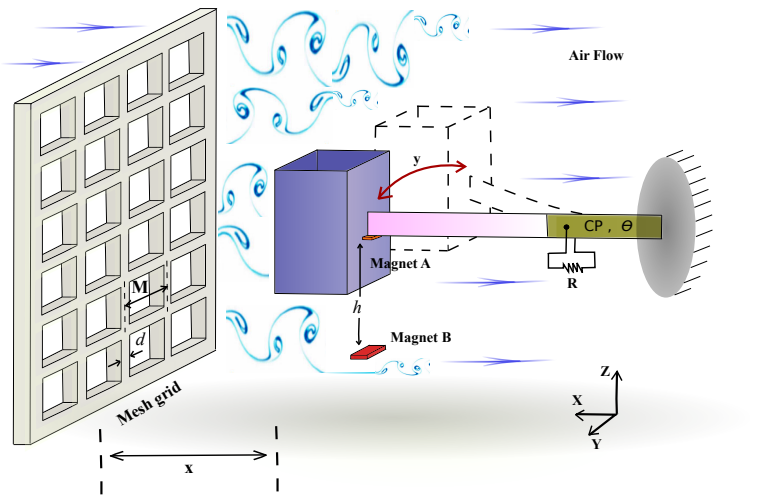

Figure 6.1: A schematic diagram of the galloping flow energy harvester and the grid used to generate turbulence.

the mesh opening, M_e which represents the distance from the center of one rod to the next, and the characteristic width of the rod, D. As shown in Fig. 6.1, these two parameters can be used to control the porosity of the grid, β, which represents the ratio between the open and total area of the screen and is given by

$$\beta = \left(1 - \frac{D}{M_e}\right)^2. \tag{6.1}$$

In this study, three different grids, A, B, and C, with different rod widths, D, and different openings, M_e, have been considered to generate the multi-frequency wake in the windward direction of the harvester. The geometric properties of the designed grids and the associated porosity are listed in Table 6.1.

To investigate the harvester's response in both of the bi-stable and linear configurations, a series of wind tunnel experiments are conducted using the experimental setup depicted in Fig. 6.2. The wind excitation is produced using a wind tunnel with air velocity tuner having a very fine speed resolution.

Four sensitive and high resolution hot-wire sensors are used to measure the air

Table 6.1: Grid geometrical properties.

Grid	$D(mm)$	$M(mm)$	$\beta(\%)$	$Re_d(\times 10^2)$
Grid A	6.35	38.1	69.4	$25.4 - 42.3$
Grid B	9.53	54.0	67.8	$38.1 - 63.5$
Grid C	12.70	63.5	64.0	$50.8 - 84.6$

velocity in at four different locations along the Y-axis as shown in Fig. 2.4. The sensors are placed in a plane below the bluff body to avoid the effect of oscillation's back pressure on the sensors' readings. A mesh screen located in the upstream of the harvester is used to generate multi-frequency vortex streets, and a laser vibrometer is used to record the tip displacement. The beam is made of a stainless steel sheet with dimensions of $190 \times 28 \times 1$ mm^3, an effective mass, m, of 0.104 Kg and a damping ratio, ζ, of 0.003. The microfiber composite (MFC) layer used to convert the strain into electric charge has dimensions of $95 \times 28 \times 0.2$ mm^3, and a capacitance, C_p,

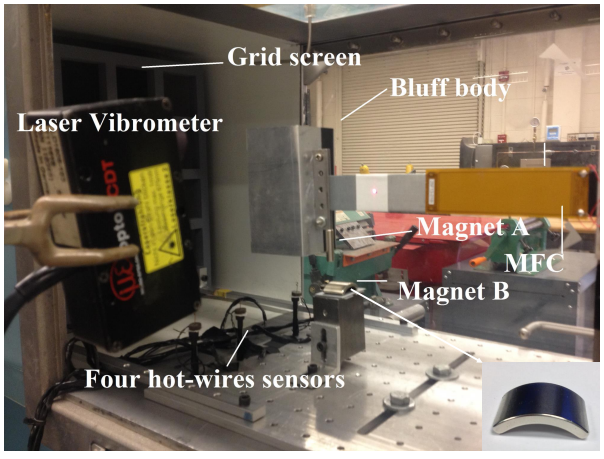

Figure 6.2: Overview of the experimental setup.

of 172 nF. A square-sectioned bluff body with dimensions of 50 $\times$ 50 $\times$ 100 mm^3 is attached to the free end of the cantilever beam and faces the flow direction. A resistor box is used to vary the resistive load, R, which is connected in parallel to the piezoelectric patch.

Two repulsive magnets A, and, B, separated by a threshold distance h, as shown in Fig. 6.1, are used to generate the bi-stable restoring force. The lower magnet, B, is chosen to be a curved magnet to reduce twist and encourage inter-well motions at relatively lower driving forces, i.e., lower wind speed. The magnet is also placed in a plane behind the bluff body on the downside and at a relatively far distance to avoid altering the flow pattern.

6.2 Response in a Uniform Flow

We first investigate the harvester's performance without the grids. Both of the linear restoring force (without magnets), and the bi-stable nonlinear restoring force (with magnets) are considered. In both scenarios, the MFC patch is connected in parallel with a fixed arbitrary chosen resistive load of 310 KΩ. The mean wind speed is approximated by averaging the data collected by the four hot-wire sensors.

Figure 6.3 depicts a comparison between the harvester's response in both configuration. It is evident that the linear harvester undergoes larger deflections at lower wind speeds. The bi-stable harvester, on the other hand, undergoes larger deflections at higher wind speeds. This occurs when the driving wind energy is large enough to allow the dynamic trajectories of the bi-stable system to escape from one potential well to the other performing inter-well oscillations. As shown in Fig. 6.3(b), these trends are not reflected in the voltage response since the linear design clearly outperforms the bi-stable one over the whole range of the wind speeds considered [61]. This is attributed to the fact that the output voltage is not only proportional to

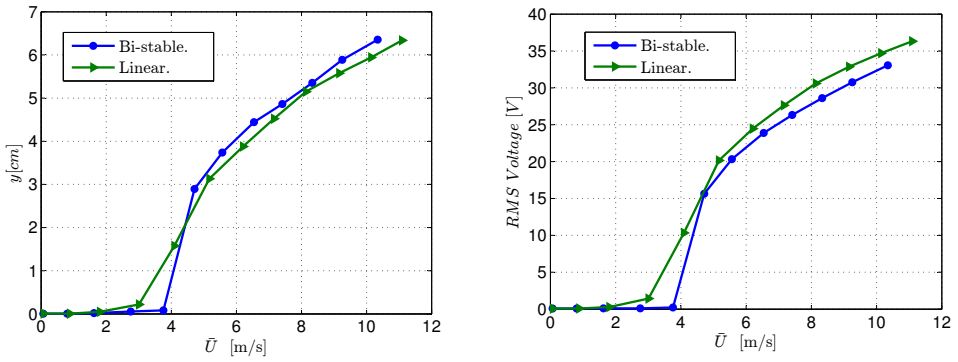

(a) (b)

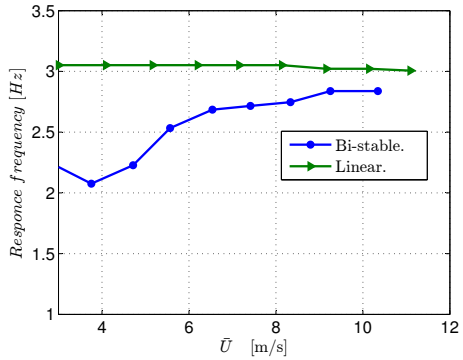

(c)

Figure 6.3: Variation of the harvester's response with the mean wind speed (no mesh in the upstream) (a) tip deflection (b) root-mean square voltage across resistive load 310 KΩ and (c) response frequency, for bi-stable (circles) and linear (triangles) systems.

the deflection, but is also proportional to the frequency of oscillations. As shown in Fig. 6.3(c), the response frequency of the bi-stable harvester drops substantially when the inter-well oscillations are activated. Due to the hardening nonlinearities, the frequency recovers as the amplitude is increased further but reaches a threshold that is still below the natural frequency of the linear system. The net effect is that the drop in frequency overcomes the increase in deflection which causes the voltage to drop.

6.3 Response in a Non-Unifrom Flow

When the kinetic energy of the mean flow is large enough the vortical structures can undergo a series of bifurcations by pumping kinetic energy from the mean flow. This kinetic energy sustains these vortical structures in space and time, which allows strong nonlinear interactions between them. These interactions can lead the flow pattern to lose its spatio-temporal coherence and eventually becomes turbulent.

The flow patterns, which involve strong and complex interferences between the wakes behind the grids, should affect the dynamics of the harvester, then the amount of energy generated. To investigate how the flow characteristics influence the harvester's performance, the harvester is placed behind the grids at different locations along the X-axis (5 cm increments). At each distance, time traces of the tip velocity and output voltage of the harvester are recorded for a mean flow speed of 10 m/s.

Before analyzing the velocity fluctuations, around the mean value, the time traces

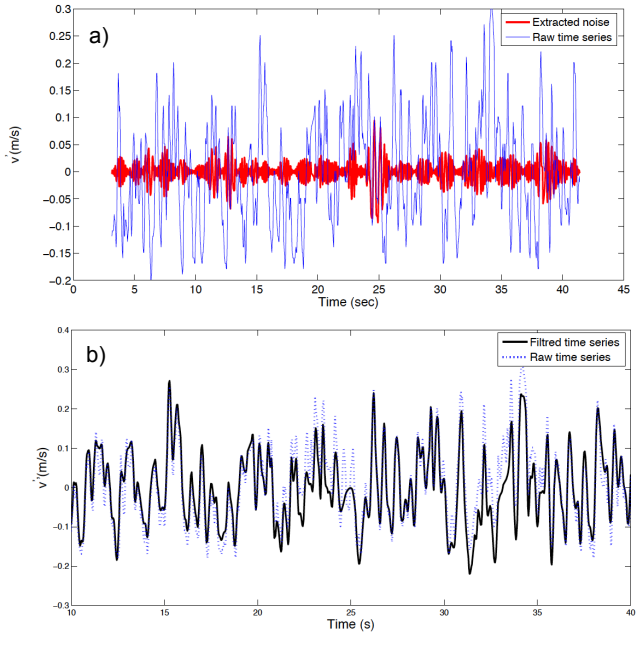

Figure 6.4: Noise filtering using empirical method decomposition (EMD)

were filtered to reduce the influence of the intrinsic measurement noise. To this end, we used the Empirical Mode Decomposition technique (EMD) [65], where only modes of significant amplitudes are considered. Modes of much smaller amplitude are considered as intrinsic noise, and, hence were filtered out. Figures 6.4 (a,b) depicts the results of the filtering procedure. Figures 6.4(a) shows the mode considered as noise (in red) which is of small amplitudes and high frequency. Figures 6.4 (b) shows the superposition of the relevant modes of the time trace and its comparison with the raw time series recorded by the hot-wire sensors.

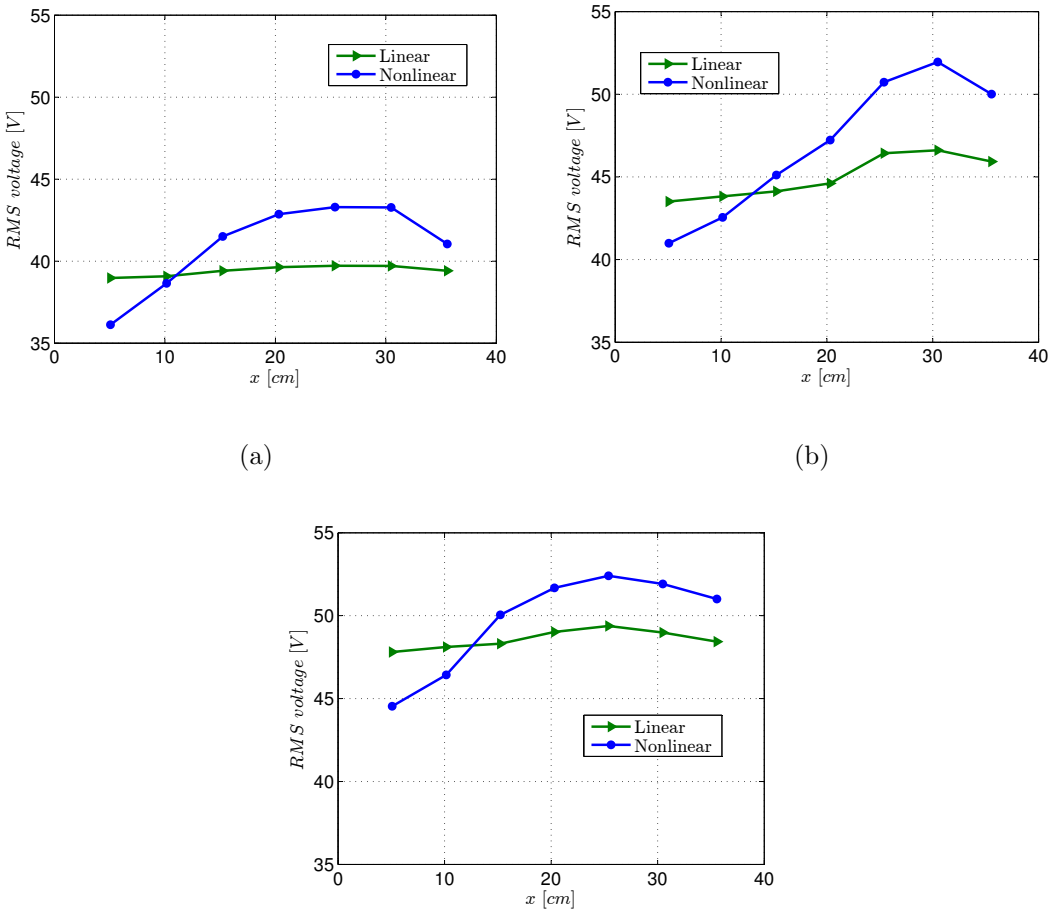

(a) (b)

(c)

Figure 6.5: voltage across resistive load of 310 KΩ of the linear and bi-stable harvester at different locations behind the grid. (a) Grid A, (b) Grid B, and (c) Grid C.

Figure 6.5 depicts the RMS voltage of the linear and nonlinear harvesters as measured at seven different locations behind the three grids. A quick inspection of the figures reveals that *i*) the flow behind Grids B and C generates higher voltage levels as compared to Grid A, *ii*) the bi-stable harvester generates higher power levels at stations which are further form the grids, and *iii*) the bi-stable harvester generates maximum voltage levels somewhere near locations 5 and 6.

To explain these findings, we utilize the Fourier transform to characterize the flow patterns. The spectrum, P_v, of the flow fluctuation for the three grids is shown in Fig. 6.6. Each figure shows a set of spectra of the velocity fluctuations measured at 4 stations over a distance of 35 cm behind the grid.

Figure 6.6 (a) shows the power spectrum of the flow fluctuation behind Grid A, which has the lowest porosity. The power spectra indicate that there are two distinct regions. The first occurs towards lower frequencies (0.1 to 2 Hz) where the fluctuation of the mean velocity exhibits a weak dependence on the frequency, f. The second regime (2 to 10 Hz) is a relatively slow rate dissipation regime following a power law, $f^{-0.3}$. In the first regime, the spectra is not monotonic, but exhibits very few clear frequency peaks. This indicates that the flow which resulted from the destabilization of the mean flow involves only very few large scale vortical structures. The spectra of the flow fluctuations at 5 cm behind the grid (loc1) contains the lowest energy indicating that vortices did not have enough time and space to pump sufficient kinetic energy from the mean flow to grow. As a result, as shown in Fig. 6.5 (a) both the linear and bi-stable harvesters produce very little power.

As shown in Fig. 6.5 (a), the level of the output voltage generated by the bi-stable harvester increases substantially as the harvester is placed further behind the grid. Maximum voltage is generated near station five (loc5) where the spectra also reveals that a powerful mode exists due to maturation of the flow structure. When comparing the linear to the bi-stable system, it becomes evident that the bi-stable

harvester outperforms the linear one except when placed very close to the grid; that is when the vortices have very little energy.

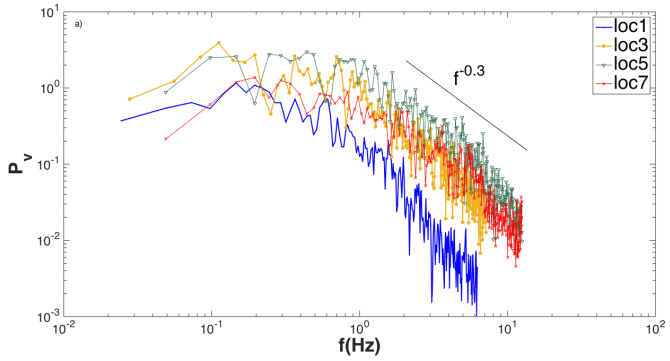

(a)

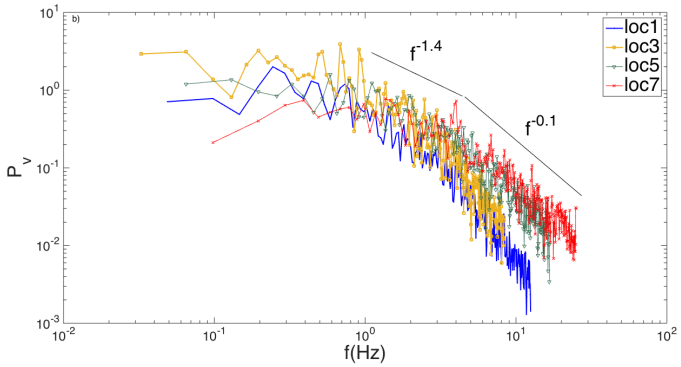

(b)

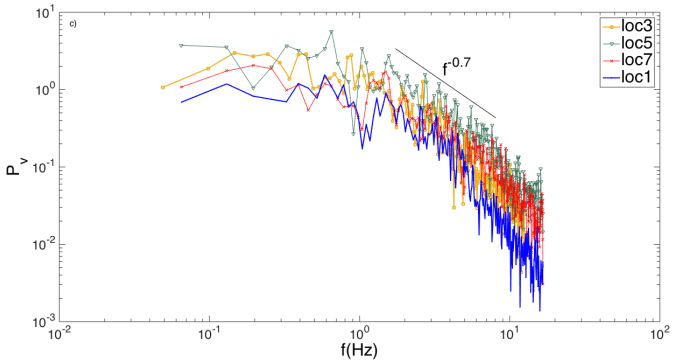

(c)

Figure 6.6: Power spectra of the velocity fluctuations at different locations behind the grid. (a) Grid A, (b) Grid B, and (c) Grid C.

Figure 6.6 (b) depicts the power spectra of the velocity fluctuation associated with Grid B. In contrast with Grid A, now the power spectra encompasses three flow regimes. The first one is a frequency independent plateau between 0.1 to 1 Hz. The second regime consists of a relatively strong interaction between the perturbation modes. This occurs in the frequency domain between 1 and 3 Hz where the cascade of energy towards small scale flow structures follows a self-similar power law decay, $f^{-1.4}$, which is close to the Kolmogorov scaling $f^{-5/3}$ of turbulent flows. The third flow regime is a power law, $f^{-0.1}$ cascade towards small scale flow structures. This cascade is relatively faster rate than the one found in the flow behind Grid A.

Near the harvester's natural frequency of 3 Hz, we notice that stations seven (loc7) then five (loc5) contains maximum energy in the form of small-scale non-linearly interacting vortices. It is in this region where the harvester is expected to respond best to the flow and hence we notice that maximum voltage is being generated between these two stations. Furthermore, we notice that the bi-stable harvester still outperforms the linear one. This is because the energy is distributed over a wide range of frequencies around 3 Hz further illustrating the insensitivity of the bi-stable harvester to frequency variations.

Figure 6.6 (c) depicts the power spectra of the fluctuation of the velocity behind Grid C. The flow pattern is very similar to the one observed behind Grid A. The spectra exhibit a broad band at low frequencies (0.1 to 1Hz) with few frequency peaks. This indicates that the flow pattern is composed of few interacting vortical structures with the dominant modes appearing between stations two (loc2) and five (loc5). In contrast with the flow behind Grids A and B, the nonlinear interactions between the fluctuation modes of the flow velocity is weak, which resulted in a slow self-similar decay, $f^{-0.7}$, between the frequency interval of 1 to 10 Hz.

Similar to Grid B, near the harvester's natural frequency of 3 Hz, we notice that stations five (loc5) then seven (loc7) contain maximum energy in the form of small-

scale non-linearly interacting vortices. It is in this region where the harvetser is expected to respond best to the flow, and, hence, we notice that maximum voltage is being generated between these two stations.

The experiments also indicate that the harvester performs significantly better behind Grids B and C. This suggests that it performs well in the presence of strong nonlinear interactions and lower rates of energy dissipation around its natural frequency. The number of modes involved in the flow behind Grid A is relatively small compared to the two others grids. This has limited the amount of kinetic energy pumped from the mean flow by the vortical structures and weakened the interactions between the modes.

Chapter 7

Conclusions

This Chapter presents the major conclusions of this Dissertation and the potential future research directions.

The research in this Dissertation focused on investigating the influence of stiffness nonlinearities on the performance of galloping FEHs. First, the performance of nonlinear galloping FEHs in a uniform flow was investigated. To maximize the output power, directions on how to design the restoring force for a given flow characteristics were also provided. Second, the influence of stiffness nonlinearities on the performance of wake-galloping energy harvesters under single- and multi-frequency vortex streets was investigated. In what follows a summary of the concluding remarks is provided.

7.1 Galloping Flow Energy Harvesting in a Uniform Flow

The influence of stiffness nonlinearities on the performance of galloping FEHs was investigated. To this end, a galloping FEH with a Duffing quartic potential func-

tion of the form $\mathcal{V} = \frac{1}{2}\mu y^2 + \frac{1}{4}\gamma y^4$ was considered. A physics-based model of the galloping FEH assuming a piezoelectric transduction mechanism and a quasi-steady aerodynamic flow field was developed. The model is subsequently validated against experimental data for the different types of restoring forces considered. A closed-form solution of the adopted model is obtained by employing the Jacobi elliptic functions and used to investigate the influence of the nonlinearity on the performance of the harvester under optimal electric loading conditions. It is shown that,

- For similar design parameters, and values (magnitude) of $\bar{\mu}$ and $\bar{\gamma}$, a FEH incorporating a softening restoring force outperforms the hardening design at the optimal loading conditions up to the point where the dynamic trajectories associated with the softening system escape from the potential barrier. Similarly, a FEH with a mono-stable hardening restoring force outperforms the bi-stable harvester as long as oscillations are confined to a single potential well, i.e., intra-well oscillations.

- For similar design parameters, and values (magnitude) of $\bar{\mu}$ and $\bar{\gamma}$, the bi-stable harvester clearly outperforms the mono-stable hardening design in the parameter space where the inter-well oscillations of the bi-stable harvester are excited.

- When two harvesters possessing the same type of restoring force, i.e. softening or hardening or bi-stable, have the same value of the design ratio $\frac{|\bar{\gamma}|}{\bar{\mu}^2}$, then the harvester with the smaller value of $\bar{\mu}$ provides higher output power levels at the same wind speed.

- When two harvesters possessing the same type of restoring force have the same value of $\bar{\mu}$ but different values of $\bar{\gamma}$, then the harvester with the smaller $\bar{\gamma}$, including the negative values, will provide higher output power levels.

7.2 Bi-stable Wake-Galloping Flow Energy Harvesters: Response to a Periodic Single-Frequency Wake

A theoretical and experimental investigation was carried out to demonstrate that, when subjected to a single-frequency periodic wake, the broadband characteristics of wake-galloping FEHs can be dramatically improved by incorporating a bi-stable restoring force. This has the influence of reducing the harvester's sensitivity to variations in the wind speed around the nominal design value. It has also been demonstrated that the shape of the potential function has a considerable influence on the performance of the bi-stable FEH. Specifically, it has been shown that, for shallower potential wells and smaller separation distances between the wells, the harvester starts performing large inter-well motions at lower wind speeds, but the resulting inter-well motions are generally smaller. On the other hand, for deeper potential wells and larger separation distances between the wells, the harvester starts performing large inter-well motions at higher wind speeds, but the magnitude of the resulting inter-well motions are generally larger.

7.3 Bi-stable Wake-Galloping Flow Energy Harvesters: Response to a Multi-Frequency Wake

This task examined the influence of the nonlinearity on the performance of a bi-stable galloping energy harvester under multi-frequency excitations and compared its performance to an equivalent linear device. To that end, a multi-frequency vortex street was generated in a wind tunnel using static-grid structures and wind tunnel experiments were carried out to compare the relative performance of the

bi-stable and linear systems. Results comparing the power harvested from both systems demonstrated that the bi-stable system performs better as long as it is placed further behind the grids. This stems from the fact that, right behind the grid, the vortices do not have sufficient time to build. Maximum voltage levels were generated at the stations where the interacting vortices result in powerful modes close to the harvester's natural frequency.

7.4 Directions for Future Research

The research carried out in this Dissertation only considered simple circuit models for the electrical subsystem. Nonlinear electrical circuits that resonate internally with the mechanical subsystem have been developed and widely used for vibration absorption purposes [66]. Therefore, incorporating more complex energy harvesting circuits might be used to further enhance the electromechanical transduction of flow energy harvesters.

Throughout this research, different shapes of nonlinear restoring force were considered. The relative performance of energy harvester employing mono-stable hardening, mono-stable softening, and bi stable restoring forces was evaluated and compared to the linear design. Since the bi-stable restoring force was shown to be superior with respect to the linear design, other, more complex, multi-stable restoring force designs can also be considered. A tri-stable (with three wells) restoring force have already been adopted for vibratory energy harvesting and shown to further improve the bandwidth and performance over the bi-stable design [67]. Hence, investigating a tri-stable galloping based FEH and comparing its performance to the bi-stable one presents an interesting topic for future research.

Finally, in this research we have only investigated the performance of nonlinear FEHs in a wind tunnel. While this step is considered an essential stride in charac-

terizing the harvester's response under different flow conditions, incorporating the actual wind statistics in a given location is very important for more accurate power predictions. This approach has been adopted for galloping energy harvesters incorporating a linear restoring force and would constitute an interesting topic of future research concerning nonlinear FEHs [68].

Bibliography

[1] Kristien Donners, Marc Waelkens, and J Deckers. Water mills in the area of sagalassos: a disappearing ancient technology. *Anatolian Studies*, 52:1–17, 2002.

[2] Adam Lucas. *Wind, water, work: ancient and medieval milling technology*, volume 8. Brill, 2006.

[3] Godfrey Boyle. *Renewable Energy*. Oxford University Press, 2004.

[4] Andries J du Plessis, Marcel J Huigsloot, and Fred D Discenzo. Resonant packaged piezoelectric power harvester for machinery health monitoring. In *Smart Structures and Materials*, pages 224–235. International Society for Optics and Photonics, 2005.

[5] Daniel J Inman and Benjamin L Grisso. Towards autonomous sensing. In *Smart Structures and Materials*, pages 61740T–61740T. International Society for Optics and Photonics, 2006.

[6] Steven W Arms, CP Townsend, DL Churchill, JH Galbreath, and SW Mundell. Power management for energy harvesting wireless sensors. In *Smart Structures and Materials*, pages 267–275. International Society for Optics and Photonics, 2005.

[7] Shad Roundy and Paul K Wright. A piezoelectric vibration based generator for wireless electronics. *Smart Materials and Structures*, 13(5):1131, 2004.

[8] Shad Roundy, Paul K Wright, and Jan Rabaey. A study of low level vibrations as a power source for wireless sensor nodes. *Computer Communications*, 26(11):1131–1144, 2003.

[9] Orhan Soykan. Power sources for implantable medical devices. *Medical Device Manufacturing & Technology*, pages 76–79, 2002.

[10] ID Capel, HM Dorrell, EP Spencer, and MWL Davis. The amelioration of the suffering associated with spinal cord injury with subperception transcranial electrical stimulation. *Spinal Cord*, 41(2):109–117, 2003.

[11] Richard S Sanders and Michel T Lee. Implantable pacemakers. *Proceedings of the IEEE*, 84(3):480–486, 1996.

[12] Gerbert J Renzenbrink and Maarten J Ijzerman. Percutaneous neuromuscular electrical stimulation (p-nmes) for treating shoulder pain in chronic hemiplegia. effects on shoulder pain and quality of life. *Clinical Rehabilitation*, 18(4):359–365, 2004.

[13] Thiago Seuaciuc-Osório and Mohammed F Daqaq. Effect of bias conditions on the optimal energy harvesting using magnetostrictive materials. In *The 15th International Symposium on: Smart Structures and Materials & Nondestructive Evaluation and Health Monitoring*, pages 69280B–69280B. International Society for Optics and Photonics, 2008.

[14] Mohammed F Daqaq, Jamil M Renno, Justin R Farmer, and Daniel J Inman. Effects of system parameters and damping on an optimal vibration-based energy harvester. In *Proceedings of the 48th AIAA/ASME/ASCE/AHS/ASC Structures, Structural Dynamics, and Materials Conference, Honolulu, HI, April*, pages 23–26, 2007.

[15] A Erturk and Daniel J Inman. An experimentally validated bimorph cantilever model for piezoelectric energy harvesting from base excitations. *Smart Materials and Structures*, 18(2):025009, 2009.

[16] Noel E DuToit and Brian L Wardle. Experimental verification of models for microfabricated piezoelectric vibration energy harvesters. *AIAA Journal*, 45(5):1126–1137, 2007.

[17] Alper Erturk and Daniel J Inman. *Piezoelectric Energy Harvesting*. John Wiley & Sons, 2011.

[18] Lihua Tang and Yaowen Yang. A nonlinear piezoelectric energy harvester with magnetic oscillator. *Applied Physics Letters*, 101(9):094102, 2012.

[19] Ravindra Masana and Mohammed F Daqaq. Relative performance of a vibratory energy harvester in mono-and bi-stable potentials. *Journal of Sound and Vibration*, 330(24):6036–6052, 2011.

[20] Zengtao Yang and Jiashi Yang. Connected vibrating piezoelectric bimorph beams as a wide-band piezoelectric power harvester. *Journal of Intelligent Material Systems and Structures*, 20(5):569–574, 2009.

[21] BP Mann and ND Sims. Energy harvesting from the nonlinear oscillations of magnetic levitation. *Journal of Sound and Vibration*, 319(1):515–530, 2009.

[22] Shengxi Zhou, Junyi Cao, Alper Erturk, and Jing Lin. Enhanced broadband piezoelectric energy harvesting using rotatable magnets. *Applied Physics Letters*, 102(17):173901, 2013.

[23] Paul D Mitcheson, Eric M Yeatman, G Kondala Rao, Andrew S Holmes, and Tim C Green. Energy harvesting from human and machine motion for wireless electronic devices. *Proceedings of the IEEE*, 96(9):1457–1486, 2008.

[24] PBS Lissaman. Low-reynolds-number airfoils. *Annual Review of Fluid Mechanics*, 15(1):223–239, 1983.

[25] M. Bryant and E. Garcia. Energy harvesting: a key to wireless sensor nodes. In *Second International Conference on Smart Materials and Nanotechnology in Engineering*, pages 74931W–74931W. International Society for Optics and Photonics, 2009.

[26] G. W. Taylor, J. R. Burns, S. Kammann, W. B. Powers, and T. R. Welsh. The energy harvesting eel: a small subsurface ocean/river power generator. *Oceanic Engineering, IEEE Journal*, 26(4):539–547, 2001.

[27] S. Pobering and N. Schwesinger. A novel hydropower harvesting device. In *MEMS, NANO and Smart Systems, 2004. ICMENS 2004. Proceedings. 2004 International Conference*, pages 480–485. IEEE, 2004.

[28] A Mehmood, A Abdelkefi, MR Hajj, AH Nayfeh, I Akhtar, and AO Nuhait. Piezoelectric energy harvesting from vortex-induced vibrations of circular cylinder. *Journal of Sound and Vibration*, 332(19):4656–4667, 2013.

[29] HD Akaydın, N Elvin, and Y Andreopoulos. Wake of a cylinder: a paradigm for energy harvesting with piezoelectric materials. *Experiments in Fluids*, 49(1):291–304, 2010.

[30] Hyung-Jo Jung and Seung-Woo Lee. The experimental validation of a new energy harvesting system based on the wake galloping phenomenon. *Smart Materials and Structures*, 20(5):055022, 2011.

[31] Matthew Bryant, Eric Wolff, and Ephrahim Garcia. Parametric design study of an aeroelastic flutter energy harvester. In *SPIE Smart Structures and Materials+ Nondestructive Evaluation and Health Monitoring*, pages 79770S–79770S. International Society for Optics and Photonics, 2011.

[32] A Erturk, WGR Vieira, C De Marqui Jr, and DJ Inman. On the energy harvesting potential of piezoaeroelastic systems. *Applied Physics Letters*, 96(18):184103, 2010.

[33] Liaosha Tang, Michael P Païdoussis, and Jin Jiang. Cantilevered flexible plates in axial flow: energy transfer and the concept of flutter-mill. *Journal of Sound and Vibration*, 326(1):263–276, 2009.

[34] Carlos De Marqui, Alper Erturk, and Daniel J Inman. Piezoaeroelastic modeling and analysis of a generator wing with continuous and segmented electrodes. *Journal of Intelligent Material Systems and Structures*, 21(10):983–993, 2010.

[35] A Bibo and MF Daqaq. Investigation of concurrent energy harvesting from ambient vibrations and wind using a single piezoelectric generator. *Applied Physics Letters*, 102(24):243904, 2013.

[36] J. Sirohi and R. Mahadik. Piezoelectric wind energy harvester for low-power sensors. *Journal of Intelligent Material Systems and Structures*, page 1045389X11428366, 2011.

[37] J. Sirohi and R. Mahadik. Harvesting wind energy using a galloping piezoelectric bceam. *Journal of Vibration and Acoustics*, 134(1):011009, 2012.

[38] Matthew Bryant and Ephrahim Garcia. Modeling and testing of a novel aeroelastic flutter energy harvester. *Journal of Vibration and Acoustics*, 133(1):011010, 2011.

[39] VC Sousa, M de M Anicézio, C De Marqui Jr, and A Erturk. Enhanced aeroelastic energy harvesting by exploiting combined nonlinearities: theory and experiment. *Smart Materials and Structures*, 20(9):094007, 2011.

[40] Antonio Barrero-Gil, G Alonso, and A Sanz-Andres. Energy harvesting from transverse galloping. *Journal of Sound and Vibration*, 329(14):2873–2883, 2010.

[41] JM Kluger, FC Moon, and RH Rand. Shape optimization of a blunt body vibro-wind galloping oscillator. *Journal of Fluids and Structures*, 40:185–200, 2013.

[42] A Abdelkefi, MR Hajj, and AH Nayfeh. Piezoelectric energy harvesting from transverse galloping of bluff bodies. *Smart Materials and Structures*, 22(1):015014, 2013.

[43] Yaowen Yang, Liya Zhao, and Lihua Tang. Comparative study of tip cross-sections for efficient galloping energy harvesting. *Applied Physics Letters*, 102(6):064105, 2013.

[44] Mohammed Daqaq, Ravindra Masana, Alper Erturk, and D Dane Quinn. On the role of nonlinearities in vibratory energy harvesting: A critical review and discussion. *Applied Mechanics Reviews*, 2013.

[45] A. Roshko. Experiments on the Flow Behind a Circular Cylinder at Very High Reynolds Numbers. *Journal of Fluid Mechanics*, 10:345–356, 1960.

[46] H D Akaydin, N Elvin, and Y Andreopoulos. The performance of a self-excited fluidic energy harvester. *Smart materials and Structures*, 21(2):025007, 2012.

[47] FC Moon and Philip J Holmes. A magnetoelastic strange attractor. *Journal of Sound and Vibration*, 65(2):275–296, 1979.

[48] S. C. Stanton, C. C. McGehee, and B. P. Mann. Nonlinear Dynamics for Broadband Energy Harvesting: Investigation of a Bistable Piezoelectric Inertial Generator. *Physica D: Nonlinear Phenomena*, 239:640–653, 2010.

[49] A. Erturk, J. Hoffmann, and D. J. Inman. A Piezomagnetoelastic Structure for Broadband Vibration Energy Harvesting. *Applied Physics Letters*, 94(25):254102, 2009.

[50] BP Mann and BA Owens. Investigations of a nonlinear energy harvester with a bistable potential well. *Journal of Sound and Vibration*, 329(9):1215–1226, 2010.

[51] Francesco Cottone, Helios Vocca, and L Gammaitoni. Nonlinear energy harvesting. *Physical Review Letters*, 102(8):080601, 2009.

[52] AM Wickenheiser and E Garcia. Broadband vibration-based energy harvesting improvement through frequency up-conversion by magnetic excitation. *Smart Materials and Structures*, 19(6):065020, 2010.

[53] Brian P Mann, David AW Barton, and Benjamin AM Owens. Uncertainty in performance for linear and nonlinear energy harvesting strategies. *Journal of Intelligent Material Systems and Structures*, page 1045389X12439639, 2012.

[54] Amin Bibo and Mohammed F Daqaq. An analytical framework for the design and comparative analysis of galloping energy harvesters under quasi-steady aerodynamics. *Smart Materials and Structures*, 24(9):094006, 2015.

[55] GV Parkinson and JD Smith. The square prism as an aeroelastic non-linear oscillator. *The Quarterly Journal of Mechanics and Applied Mathematics*, 17(2):225–239, 1964.

[56] S Granger and MP Paidoussis. An improvement to the quasi-steady model with application to cross-flow-induced vibration of tube arrays. *Journal of Fluid Mechanics*, 320:163–184, 1996.

[57] A Bibo and MF Daqaq. On the optimal performance and universal design curves of galloping energy harvesters. *Applied Physics Letters*, 104(2):023901, 2014.

[58] A. H. Nayfeh. *Introduction to Perturbation Techniques*. John Wiley & Sons, 2011.

[59] P. Mitcheson, E. Yeatman, K. Rao, S. Holmes, and T. Green. Energy Harvesting from Human and Machine Motion for Wireless Electronic Devices. *Proceedings of the IEEE*, 96:1457–1486, 2008.

[60] P. Lissaman. Low-Reynolds-Number Airfoils. *Annual Review in Fluid Mechanics*, 15:223–239, 1983.

[61] Ali H Alhadidi, Amin Bibo, and Mohammed F Daqaq. Flow energy harvesters with a nonlinear restoring force. In *ASME 2014 Conference on Smart Materials, Adaptive Structures and Intelligent Systems*, pages V002T07A006–V002T07A006. American Society of Mechanical Engineers, 2014.

[62] CHK Williamson and R Govardhan. Vortex-induced vibrations. *Annu. Rev. Fluid Mech.*, 36:413–455, 2004.

[63] H Nakaguchi, K Hashimoto, and S Muto. An experimental study on aerodynamic drag of rectangular cylinders. *J. Jpn. Soc. Aeronaut. Space Sci*, 16(1):1–5, 1968.

[64] AL Kistler and T Vrebalovich. Grid turbulence at large reynolds numbers. *Journal of Fluid Mechanics*, 26(01):37–47, 1966.

[65] Norden E Huang, Zheng Shen, Steven R Long, Manli C Wu, Hsing H Shih, Quanan Zheng, Nai-Chyuan Yen, Chi Chao Tung, and Henry H Liu. The Empirical Mode Decomposition and The Hilbert Spectrum for Nonlinear and Non-stationary Time Series Analysis. In *Proceedings of the Royal Society of London A: Mathematical, Physical and Engineering Sciences*, volume 454, pages 903–995. The Royal Society, 1998.

[66] Shafic S Oueini, Char-Ming Chin, and Ali H Nayfeh. Dynamics of a cubic nonlinear vibration absorber. *Nonlinear Dynamics*, 20(3):283–295, 1999.

[67] Shengxi Zhou, Junyi Cao, Daniel J Inman, Jing Lin, Shengsheng Liu, and Zezhou Wang. Broadband tristable energy harvester: Modeling and experiment verification. *Applied Energy*, 133:33–39, 2014.

[68] Mohammed F Daqaq. Characterizing the response of galloping energy harvesters using actual wind statistics. *Journal of Sound and Vibration*, 357:365–376, 2015.